Coating of zeolite nanosheets

A Thesis
SUBMITTED TO THE FACULTY OF
UNIVERSITY OF MINNESOTA
BY

Wanlu Zhang

IN PARTIAL FULFILLMENT OF THE REQUIREMENTS
FOR THE DEGREE OF
MASTER OF SCIENCE IN CHEMICAL ENGINEERING

Lorraine Francis, Michael Tsapatsis

May 2014

## Acknowledgements

I would like to acknowledge my advisors, Professor Lorraine Francis and Michael Tsapatsis, for providing me guidance and advises during my research.

I would like to thank my colleagues for their help and encouragement for my experiments. In particular I am grateful to Kumar Varoon Agarwal, Neel Rangnekar, Meera shete, Mi Young Jeon, Kyle Price, Bryce Williams, Garrett Swindlehurst and Limin Ren.

I would like to thank Wieslaw Suszynski for training and many helpful discussions relating to spin coating procedure and optical microscope.

Finally, I would like to thank all my friends here and my parents for their endless support.

**Abstract**

Zeolites are microporous crystalline aluminosilicates that are widely used as catalysts in petrochemistry and fine-chemical synthesis. While bulk zeolites can be used as catalysts and adsorption materials, thin zeolite films are suitable for applications such as catalytic membrane reactors, molecular sieve membranes and low-dielectric-constant materials.

Zeolite nanosheets are silicate or aluminosilicate crystals with thicknesses on the order of one layer of the crystal structure (i.e., ~2 nm) and much larger lateral dimensions (i.e., ~10-100 nm). Nanosheets contain ordered molecular scale pores that are aligned through the sheet thickness. Compared with isotropic zeolites, synthesis of thin zeolite films using high-aspect-ratio zeolite nanosheets has more advantages with packing and processing.

The overall goal of this research is to make coatings of zeolite nanosheets. To prepare the nanosheets, multilamellar MFI is synthesized as a precursor. Melt blending is applied to exfoliate the layered zeolite to achieve a polystyrene nanocomposite. A density gradient centrifugation process followed to purify the exfoliated zeolite nanosheets is able to remove both the polystyrene and the unexfoliated zeolite completely. After a suspension of zeolite nanosheets is produced, drop coating and spin coating are explored as the coating methods.

Comparisons between these two coating methods are made after characterization of these films. For the drop coating method, drying temperature is varied and controlled to study its influence on the quality of zeolite films since it is a key factor for alignment of plate-like particles during sedimentation. For the spin coating method, spin rate is one of the most important operating parameters. Therefore, different spin rates accompanied with different dwell times are chosen for study when other parameters stayed the same.

To ensure the removal of polystyrene and unexfoliated zeolite nanosheets, the purified MFI zeolite nanosheets are imaged by transmission electron microscopy. Surface information of the zeolite nanosheets films is characterized by scanning electron

microscopy and optical microscope. The degree of particle orientation, close packing and surface coverage are determined from their images. Out-of-plane and in-plane X-ray diffraction data are recorded and analyzed to give more quantitative information about the orientation of the coatings.

**Table of Contents**

iv

**List of Tables**

# List of Figures

## List of abbreviations

TEM: Transmission electron microscopy

SEM: Scanning electron microscopy

XRD: X-ray diffraction

OSDA: Organic structure directing agent

PTFE: Polytetrafluoroethylene

TEOS: Tetraethyl orthosilicate

FIB: Focused ion beam

# 1 Introduction

## 1.1 Problems specification

Zeolites are microporous crystalline aluminosilicates comprising a uniform network of $SiO_2$ and $Al_2O_3$ tetrahedra and are widely used in the field of petrochemistry and fine-chemical synthesis[1]. While bulk zeolites can be used as catalysts and adsorption materials, thin zeolite films are suitable for applications such as catalytic membrane reactors, molecular sieve membranes and low-dielectric-constant materials[2-4].

Two kinds of materials can be chosen for thin zeolite films fabrication, isotropic zeolite particles and zeolite nanosheets. Zeolite nanosheets are silicate or aluminosilicate crystals with thicknesses on the order of one layer of the crystal structure (i.e., ~2 nm) and much larger lateral dimensions (i.e., ~10-100 nm). Nanosheets contain ordered molecular scale pores that are aligned through the sheet thickness. Compared with isotropic zeolite, thin zeolite films utilizing high-aspect-ratio zeolite nanosheets provide orientation control and close packing. Therefore, zeolite nanosheets will be chosen in this thesis as the operating materials.

To make high-aspect-ratio zeolite nanosheets, Choi et al.[1] developed a method to synthesize stable multilamellar MFI zeolite. A diquaternary ammonium-type surfactant was designed to direct the formation of multilamellar MFI structure. They were able to make a multilamellar stacking of MFI nanosheets with a gel composition of 30 $Na_2O$: 1 $Al_2O_3$: 100 $SiO_2$: 10 $C_{22-6-6}Br_2$: 18 $H_2SO_4$: 4000 $H_2O$.

Exfoliation of the lamellar zeolite is required to achieve intact, segregated nanosheets. Researchers in Michael Tsapatsis' group[9] developed a method to swell MCM-22 (P), the precursor to zeolite MCM-22, at room temperature without altering its layer structure drastically. The increased interlayer spacing after swelling made it possible for polymer chains intercalation. Therefore, the researchers were able to demonstrate the feasibility of polymer nanocomposites concept for making exfoliated morphology of MCM-22 layers.

In their later studies, both MWW and MFI zeolite nanosheets were successfully exfoliated by making polymer-nanosheets nanocomposites. Dissolution of nanocomposites in toluene followed by a one-step centrifugation removed unexfoliated particles. The dispersion after large particle removal was used to fabricate membranes, followed by a mild hydrothermal treatment to remove polymer.

However, polymer removal by heat treatment causes curling and agglomeration of nanosheets, requiring an improved purification procedure. To this end, Agrawal et al.[2] applied a density gradient centrifugation method. This method was able to remove polystyrene and unexfoliated zeolites completely before film fabrication. The researchers coated the purified MFI nanosheets on an alumina support using vacuum assisted filtration method, creating a compact, b-oriented, 80 nm thick film.

Although a compact and oriented film can be made using previously developed procedure, new coating methods are still in demand for making perfectly packed nanosheet coatings. Vacuum assisted deposition is feasible only on porous supports and even then it does not provide well packed layers.

So the research of this thesis focuses on coating segregated zeolite nanosheets and aims to make thin, uniform and oriented zeolite nanosheets films. A coating method can be selected from dip coating[6], spin coating, Langmuir-Blodgett deposition[7], filtration[8] and layer-by-layer deposition[9].

Spin coating and drop coating method are studied here. In principle these two coating methods can be used for all kinds of substrates. Spin coating method is a mature batch process that centrifugal force acts on the spin liquids to create uniform films and the final film thickness can be easily controlled with many existing models. Parameters such as spin rate will vary to clarify how they influence the final structure of the films. Drop coating method is an operationally simple coating method that can conserve all the particles delivered on the substrate. Emphasis will be laid on how drying conditions

affect the films. To check the degree of purity and crystallinity of exfoliated MFI zeolite nanosheets, transmission electron microscopy will be used. Scanning electron microscopy and optical microscopy will be adopted simultaneously for surface investigation of coatings. Out-of-plane and in-plane X-ray diffraction data will be recorded and analyzed to give information about coatings orientation.

# 2 Theoretical considerations

## 2.1 Spin coating

### 2.1.1 General description and mathematic models

Spin coating is a widely used coating method for preparing thin and uniform films of different kinds of materials on planar substrates. It is a batch process used significantly in the microelectronics industry[10, 11]. The process of spin coating can be divided into four stages[12, 13]: deposition, spin-up, spin-off and evaporation.
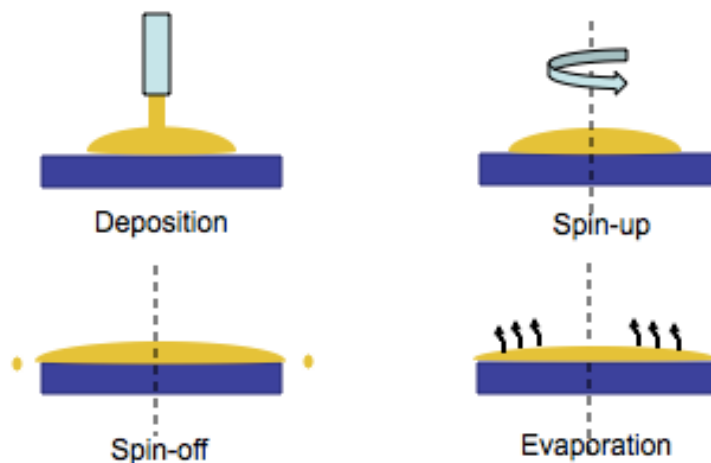


Fig 2.1 Four stages of spin coating

During deposition, an excess coating liquid is delivered on the substrate while the substrate is being static or rotating at a low speed. During spin-up, the substrate gradually accelerates to its setting speed. The spin-up time is usually very short. Spin-off stage is when the substrate rotates at its operating speed and liquid flies off radially. When the liquid thins to a certain point, convective outflow driven by centrifugal force ceases because the viscosity of the liquid increases drastically due to evaporation of the solvent. The first three stages happen sequentially. Evaporation occurs during the entire process, but its importance depends on the vapor pressure of the solvent and environmental conditions during the first three steps. It occurs independently at the end of spin coating process.

The spin coating method is able to produce a very thin film and can easily control the final film thickness. To analyze this problem, existing mathematic models describing different spin solutions or suspensions can be utilized[14-19]. The mathematic models relate the dry film thickness to several operating parameters and the properties of the spinning materials. For instance, the final spin speed, the total spin time, the coating liquid's viscosity, density and vapor pressure are all key variations that should be taken into account when determining the resulting film thickness.

Emslie et al. gave simple equations describing the flow of a Newtonian liquid on the rotating disk by equating viscous force and centrifugal force along the radius of disk[15]. In the equations, it is assumed that the rotating plane is infinite, the plane is horizontal, the liquid dispersing on the disk is Newtonian. Additionally, the liquid layer is very thin so that shear resistance is not taken into consideration elsewhere besides in the horizontal planes and Coriolis force can be neglected.

Below is the development of the mathematical model for film thickness based on the above assumptions. First, viscous and centrifugal forces are equated on a per unit volume basis

$$-\eta \frac{\partial^2 v}{\partial z^2} = \rho \omega^2 r \qquad (2.1)$$

where $\omega$ is the angular velocity, $\eta$ is the viscosity of the liquid and $\rho$ is the density of the liquid[15].
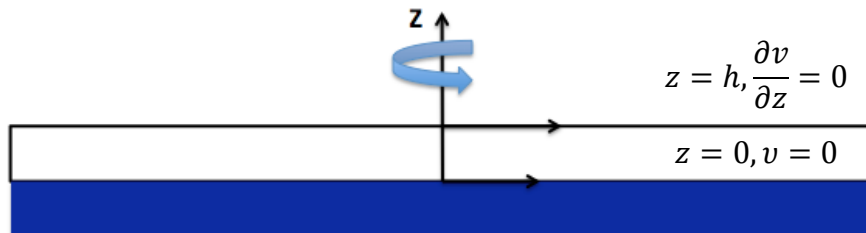


Fig 2.2 Boundary conditions for velocity profile

Boundary conditions: z=0, v=0;

5

z=h, $\frac{\partial v}{\partial z} = 0$ at the free surface

Integrate

$$\frac{\partial v}{\partial z} = -\frac{\rho\omega^2 r}{\eta}z + C_1$$

$$v = -\frac{1}{2}\frac{\rho\omega^2 r}{\eta}z^2 + C_1 z + C_2 \tag{2.2}$$

Substitute boundary condition

$$C_2 = 0$$

$$0 = -\frac{\rho\omega^2 r}{\eta}h + C_1$$

$$v = -\frac{1}{2}\frac{\rho\omega^2 r}{\eta}z^2 + \frac{\rho\omega^2 r}{\eta}hz \tag{2.3}$$

The radial flow q per unit length of circumference is

$$q = \int_0^h v\,dz = \int_0^h (-\frac{1}{2}\frac{\rho\omega^2 r}{\eta}z^2 + \frac{\rho\omega^2 r}{\eta}hz)dz$$

$$= \int_0^h d(-\frac{1}{6}\frac{\rho\omega^2 r}{\eta}z^3 + \frac{\rho\omega^2 r}{2\eta}hz^2)$$

$$= \frac{1}{3}\frac{\rho\omega^2 r}{\eta}h^3 \tag{2.4}$$

Apply equation of continuity

$$r\frac{\partial h}{\partial t} = -\frac{\partial(rq)}{\partial r} = -\frac{\partial\left(r\frac{1}{3}\frac{\rho\omega^2 r}{\eta}h^3\right)}{\partial r} \tag{2.5}$$

Assume h is not a function of r i.e. film is radially uniform

$$\frac{\partial h}{\partial t} = -\frac{2\rho\omega^2 h^3}{3\eta} \tag{2.6}$$

Initial condition: t=0 h=h_0

Integrate

$$-\frac{1}{2}\frac{1}{h^2} = -\frac{2\rho\omega^2}{3\eta}t + C$$

Substitute initial condition

$$C = -\frac{1}{2}\frac{1}{h_0^2}$$

$$h_{wet} = \frac{1}{\sqrt{\frac{1}{h_0^2} + \frac{4\rho\omega^2}{3\eta}t}} \qquad (2.7)$$

Meyerhofer's model[20] introduced solvent evaporation into Emslie et al.'s model. As solvent evaporates, the liquid's viscosity rises and film thinning by convective outflow slows and ultimately stops. Meyerhofer assumed that the film ceases flow when the rate of film thinning by convective flow equals the evaporation rate. After this point, the film thinning depends only on evaporation. The evaporation rate is $k(x_{A0} - x_{A\infty})$. $k$ is the mass-transfer coefficient.

Equating the rate of film thinning by convective flow to the evaporation rate, the wet film thickness when film ceases radially outflow is

$$\frac{\partial h}{\partial t} = -\frac{2\rho\omega^2 h^3}{3\eta} = -k(x_{A0} - x_{A\infty})$$

$$h_{wet} = [\left(\frac{3\eta}{2\rho\omega^2}\right) k(x_{A0} - x_{A\infty})]^{1/3} \qquad (2.8)$$

To calculate the mass-transfer coefficient, Kreith et al.[21] correlated the mass-transfer coefficient to other material properties.

$$k = \left(\frac{CD_g}{v_g^{1/2}\rho}\right)\left(\frac{p_A^* M_A}{RT}\right)\omega^{1/2} \qquad (2.9)$$

C is a constant depends on Schmidt number[21]

| Sc | 0.74 | 1.0 | 2.5 | 5.0 | 7.5 | 10 |
|----|------|-----|-----|-----|-----|----|
| C  | 0.33 | 0.39 | 0.60 | 0.80 | 1.0 | 1.1 |

To deduce the mass-transfer coefficient, in laminar flow regime

$$Sh = CRe^{0.5}$$

$$Sh = \frac{kr}{D_g}$$

$$Re = \frac{\omega r^2}{v_g}$$

$$\therefore k_g = CD_g\left(\frac{\omega}{v_g}\right)^{1/2} \tag{2.9}$$

$$m_A = k_g\left(\rho_A^g - \rho_{A\infty}\right) \tag{2.10}$$

Assume the gas is ideal and use Raoult's Law to describe the mixing behavior

$$\rho_A^g - \rho_{A\infty} = \frac{(p_A - p_{A\infty}) \cdot M_A}{RT} \tag{2.11}$$

$$p_A = p_A^* x_A \tag{2.12}$$

Substitute (2.9), (2.11), (2.12) into (2.10)

$$\therefore m_A = CD_g\left(\frac{\omega}{v_g}\right)^{1/2}\frac{(x_A - x_{A\infty}) \cdot p_A^* M_A}{RT}$$

$$= \rho k (x_A - x_{A\infty}), \quad k = \frac{CD_g(\omega/v_g)^{1/2}}{\rho}\frac{p_A^* M_A}{RT} \tag{2.13}$$

The solvent of zeolite nanosheets suspension is octanol in later experiments. The concentration of zeolite nanosheets is less that 0.5wt%. Meanwhile, octanol has a very low vapor pressure at room temperature (at 25 °C, vapor pressure of octanol is 9.91 Pa). During the spinning, assumption has been made that film thinning due to solvent evaporation can be ignored. Therefore, most of the assumptions made in Emslie et al.'s model can be applied to experiments conducted in this thesis. Mathematic model (2.7) instead of (2.8) is used to predict the final wet film thickness.

To get the dry film thickness

$$\frac{h_{zeolite}}{h_{wet}} = \frac{V_{zeolite}/Area}{V_{wet}/Area} = \frac{V_{zeolite}}{V_{wet}}$$

$$= \frac{m_{zeolite}/\rho_{zeolite}}{m_{wet}/\rho_{wet}}$$

$$= \frac{\rho_{wet}}{\rho_{zeolite}} \cdot \frac{m_{zeolite}}{m_{wet}}$$

$$= \frac{\rho_{wet}}{\rho_{zeolite}} \cdot mass\ concentration$$

Assume density of suspension is the same as the density of octanol

$$\frac{\rho_{wet}}{\rho_{zeolite}} = \frac{0.8279\ g/cm^3}{2\ g/cm^3}$$

$$h_{zeolite} = \frac{0.8279 \, g/cm^3}{2 \, g/cm^3} \cdot mass \; concentration \cdot h_{wet} \qquad (2.14)$$

With equation (2.7) and (2.14), the dry film thickness can be predicted based the concentration of the starting suspension, physical properties of the organic solvent and the starting film thickness.

Table 2.1 Prediction of spin coating films

| Con. (%) $h_{dry}$ (nm) $h_{wet}$ (nm) | 0.005 | 0.5 | 1 | 5 |
|---|---|---|---|---|
| 3444 | 0.071 | 7.128 | 14.256 | 71.280 |
| 1723 | 0.036 | 3.570 | 7.132 | 35.660 |
| 200 | 0.004 | 0.414 | 0.828 | 4.140 |
| 100 | 0.002 | 0.207 | 0.414 | 2.070 |
| 50 | 0.001 | 0.103 | 0.207 | 1.030 |
| 30 | 0.0006 | 0.062 | 0.124 | 0.620 |

## 2.1.2 Instrument



Fig 2.3 Model WS-650MZ-23NPP Spin coater used in the experiment

The spin coater is put horizontally in the fume hood for experiment. A leveler is put on the sample stage to ensure the planarization of the substrate. The spin coater needs to connect with two tubes. One tube connects with nitrogen, and the other connects with a vacuum pump. The nitrogen flow creates an air free zone for coating. The vacuum pump can mount the substrate on the coater during spinning in case the sample flies off. There is also an O-ring in the center that helps sealing the gap between the substrate and the coater.

## 2.2 Drop coating

Drop coating is an easy process of depositing drops of liquid on a substrate, and then allowing the solvent to evaporate.
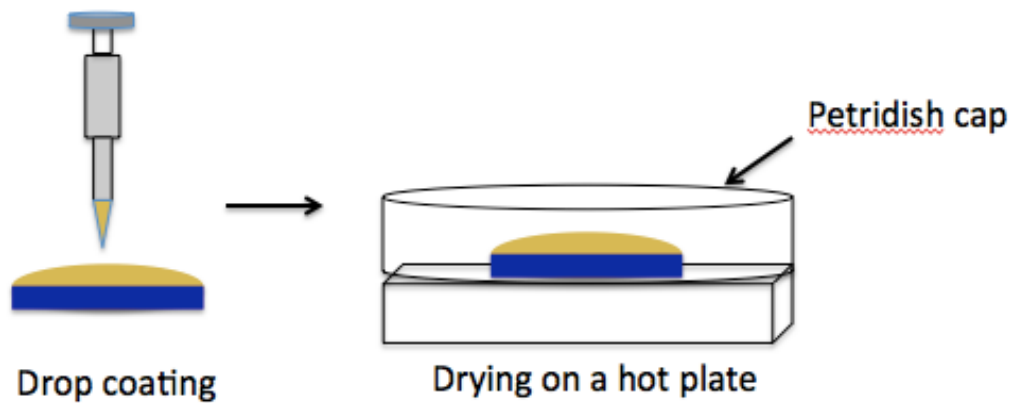


Fig 2.4 Drop coating process

### 2.2.1 Coffee-ring effects

When liquid containing particles is dropped on a substrate and evaporates, a ring-like deposit may form along the periphery. This phenomenon is quite common for drop coating and is noticeable for many dropped materials such as graphene oxide and monolayer titania[22]. According to Robert et al.[23], the coffee-ring effects are caused by capillary flow. Based on his explanation, liquid evaporating from the edge would be replenished by liquid from the inner area because of pinning of the drop/substrate contact front line. So during the evaporation of the liquid, there would form an outward flow that

carries particles to the edge. The researchers built a model and reached the conclusion that the ring mass accumulation does not depend on types of the substrate, the fluid and the particles dispersed. Therefore, this situation can also happen for the coating systems in this thesis.
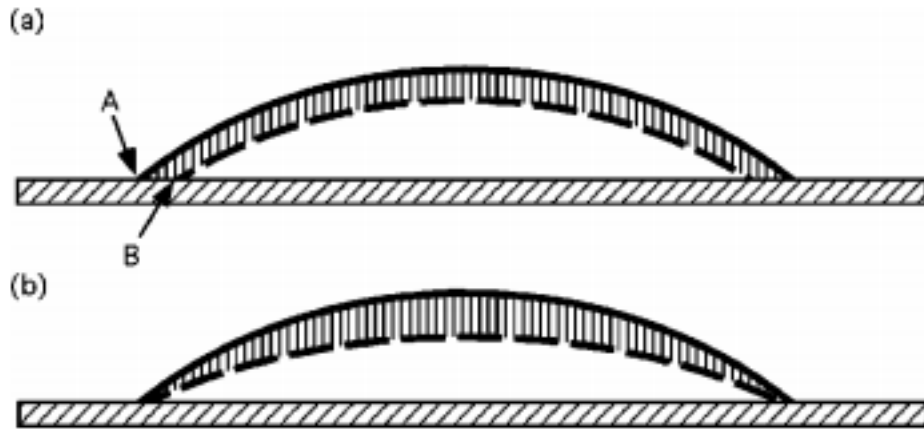


Fig 2.5 Schematic illustration of the origin of lateral flow. (a) When the contact line is not pinned, uniform evaporation makes the interface move from solid line to dashed line and the contact line will move from A to B. (b) When the contact line is pinned, the motion from A to B will be prevented by an interior outflow.[24]

## 2.2.2 Wettability of the surface of the substrate

When a liquid is dropped on a solid substrate, the degree of wetting depends on the properties of the liquid and solid. There is an adhesive force between the liquid and the solid that causes the spreading, and a cohesive force causes a drop to form a circular boundary. The contact angle at which the liquid-vapor interface meets the liquid-solid interface is determined by the force balance between the adhesive and the cohesive forces. The contact angle has an inverse relationship with wettability[25].

Table 2.2[26] Contact angle relating to degree of wetting

| Contact angle | Degree of wetting |
|---|---|
| $\theta = 0$ | Perfect wetting |
| $0 < \theta < 90°$ | High wettability |
| $90° \leq \theta < 180°$ | Low wettability |
| $\theta = 180°$ | Perfect non-wetting |
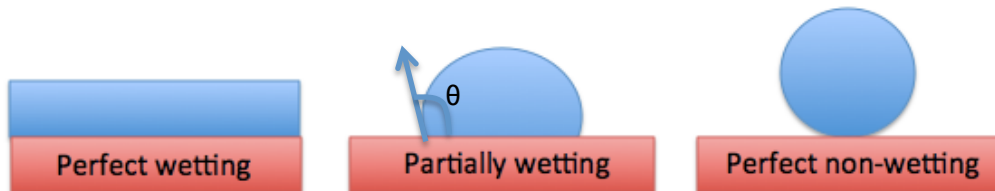


Fig 2.6 Degree of wetting

If a flat solid surface is used, Young equation can be applied[27],

$$\gamma_{SG} = \gamma_{SL} + \gamma_{LG}\cos\theta \qquad (2.15)$$

where $\gamma_{SG}$ is the surface tension between solid phase and gas phase, $\gamma_{SL}$ is the surface tension between solid phase and liquid phase, $\gamma_{LG}$ is the surface tension between liquid phase and gas phase, and $\theta$ is the contact angle.

Equation (2.15) relates the surface tension between the three phases. If by measurements, surface tension between the three phases can be found, this equation can be used to predict the contact angle for a drop of liquid that is delivered on a solid substrate. The value of contact angle therefore determines the degree of wettability.
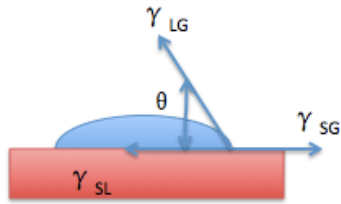
Fig 2.7 Young equation relating surface tension between the three phases[27]

In the case of making zeolite nanosheets coatings, zeolite nanosheets are dispersed in an organic solvent such as octanol. An organic solvent can easily wet a hydrophobic solid surface while it cannot easily wet a hydrophilic one. If the substrate is hydrophilic and zeolite nanosheets suspension has a very hard time to spread, drops of suspension instead of a continuous liquid may form when delivered on the substrate. The zeolite particles sediment only within a narrow area of the substrate or voids may be detected within the coating. Thus for the purpose of making a uniform coating, the substrate has to be modified to become hydrophobic before processing.

## 2.2.3 Particle orientation during drying

Drying is another important part of the drop coating method. How particles pack during the drying process determines the orientation of the coating. There are three alignment mechanisms during the drying process: film shrinkage, alignment at the substrate and alignment at the free surface[28].

Film shrinkage[29] is a common mechanism that has a great effect on flake-like particles orientation. During evaporation of the solvent, the volume of the solvent decreases and the particles are forced to orient more parallel to the flat support. This mechanism is mostly important when considering suspension with highly-viscous solvents and large particles. For other cases, disalignment mechanisms such as Brownian motion may become dominant and compensate the film shrinkage effect.

Alignment at the substrate occurs when the density of the particles is higher than the solvent and the evaporation rate of the solvent is relatively slow. In this case, the particles tend to orient perpendicular to the direction of sedimentation. If they change the alignment, there will be a pressure gradient that pushes them back to the original orientation.

Alignment at the free surface happens when the solvent evaporates at a high speed during drying and the particle has a comparatively small density. The rate of thinning the film is faster than the rate of particle sedimentation. In this case, the particles accumulate at the free surface between the solvent and the environment. High-aspect-ratio particles have an intention to orient parallel to the interface and thus parallel to the substrate.

Disalignment mechanisms contain rotational Brownian motion[30], diffusion and aggregation. Brownian motion influence depends on a different ratio of times: a characteristic time to orient the flake-like particles divided by a time to disorient them[31]. The time to orient the particles is attributed to the reciprocal of shear rate. The time to disorient them is the reciprocal of rotational diffusion coefficient $D_r$, for a disk $D_r = \frac{3k_BT}{4\mu d^3}$, d represents the diameter of the disk. From this model, it is evident that Brownian motion becomes important when the particles are small and the solvent has low viscosity. In this case particles can rotate freely in the solvent with no restraints. Diffusion happens when particles sediment or accumulate at the free surface to create an apparent concentration gradient. Due to this concentration gradient, particles diffuse from higher concentration to lower concentration. Temperature is a crucial parameter that affects diffusion rate. When the temperature is higher, the diffusion becomes more dominant. Aggregation is caused by the attractive force between particles. This attractive force varies for different solutions and suspensions.

**Drying system**

In this experiment, the coatings were put on a hot plate for drying. To calibrate the temperature on the hot plate, a thermometer was used.
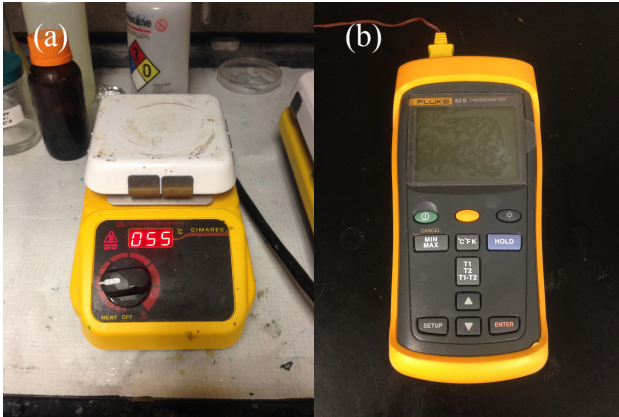


Fig 2.8 (a) Hot plate used in the experiment for drying coating (b) thermometer used for calibrating temperature on the hot plate

# 3 Characterization methods

## 3.1 SEM

### 3.1.1 General description

To get surface images of zeolite nanosheets coatings, scanning electron microscopy (SEM) was used. SEM produces a focused beam of electrons to scan the sample. The electrons interact with atoms of the sample and then yield detectable signals about the sample's surface topography and composition.

A scanning electron microscope contains an electron optical column, a vacuum system, electronics and software. Typically in an SEM, an electron beam is emitted from an electron gun fitted with a tungsten filament cathode. The electron beam normally has an energy ranging from 0.2 keV to 40 keV. The beam travels through the column by passing through several condenser lenses and deflection coils and then interacts with the sample. To prevent electron scattering from gas molecules, a sufficient vacuum level is necessary in SEM column. Therefore, the SEM column is evacuated by vacuum system before imaging. Interaction between the electron beam and the specimen causes high-energy electrons reflection, secondary electron emission, electromagnetic radiation emission, beam current absorption and etc. The electron current leaving the sample is collected, amplified and used to modulate the brightness of a cathode-ray tube. If any property of the sample causes the current leaving it to change from point to point, the image built up on the cathode-ray tube reflects this property variation over the scanned area.

Normally, samples to be imaged should be electrically conductive for SEM, or at least at the surface. Therefore, nonconductive specimens generally need to be coated with an ultrathin coating of electrically conducting materials before doing the SEM scan. The conducting materials that can be utilized include gold, platinum, osmium[32], tungsten and graphite. The thickness of the conducting film is always in the range of a few angstroms, which is thick enough for conducting but thin enough for electron penetration of the sample.

The resolution of the SEM depends on the wavelength of the electrons, the electron-optical system producing the scanning beam and the interaction volume of the electron beam and the sample. Magnification of the scanned sample depends on the ratio of the showed image size to the actual scanned area size. Compared with transmission electron microscopy (TEM), the energy of the SEM beam is not high enough to image distinguished atoms. However, SEM can image comparatively large areas of the sample and thus give surface topographic information of a film-like specimen.

The SEM instrument used in this work is the Field Emission Gun Scanning Electron Microscope JEOL 6700 in Characterization Facility of University of Minnesota. It is equipped with cold field-emission gun and has a magnification range from 10 X to 700,000 X and an ultimate resolution of 1.0 nm.

## 3.1.2 Sample preparation

As a substrate, one-inch silicon wafer as a whole was inserted into the SEM chamber. Since the zeolite nanosheet films were not conductive, 50 angstroms platinum was coated on top of the zeolite nanosheets coatings before imaging. The JEOL 6700 SEM instrument was operated at 1.5 kV and 10 A.
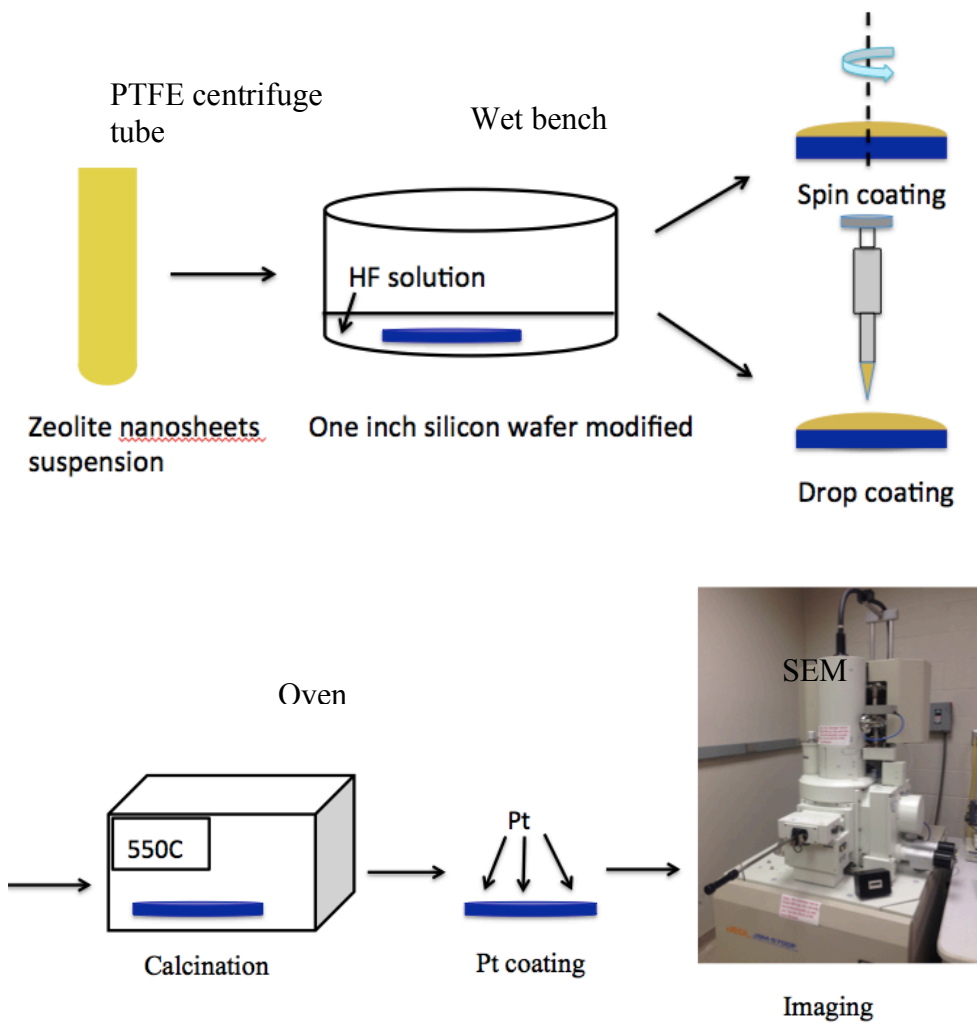
Fig 3.1 Sample preparation procedure for SEM

## 3.2 TEM

### 3.2.1 General description

Transmission electron microscopy (TEM) can be applicable in many areas such as nanotechnology, materials sciences, medical and biological research[33, 34]. It can present topographical, morphological, compositional and crystalline information of a certain material[35].

In general, a TEM is composed of an emission source, a vacuum system, a specimen stage, an electron gun, electron lenses and apertures. The whole system can be divided into three sections based on their functions[36]: the illumination system, the specimen stage and the imaging system.

The illumination system contains the electron gun and several condenser lenses. The emission source can be a tungsten filament or a lanthanum hexaboride source[35]. The electron gun emits electrons by either thermionic or field electron emission into the vacuum. A thermionic source produces electrons when heated, whereas a field-emission source produces electrons when the electric field is applied. TEM beam energies are in the range from 100 to 400 keV. The specimen stage is designed for inserting a sample holder into the chamber. The mechanical stability of the specimen stage can determine the spatial resolution of the TEM images. The imaging system comprises electron lenses that can create a magnified image of the sample on the screen. The imaging system determines the magnification of the images while the properties of the imaging lenses can decide the obtained spatial resolution for the TEM instrument.

By adjusting the magnetic lenses such that the back focal plane of the lenses is placed on the imaging apparatus, a diffraction pattern can be generated using TEM. For a single crystal, the image consists of a pattern of dots. While for polycrystalline and amorphous material, the diffraction pattern is a series of rings.

Theoretical resolution of TEM lens is given by the equation:

$$r_{th} = 0.61 \frac{\lambda}{\beta}$$

where $\lambda$ is the wavelength of the beam, $\beta$ is the semiangle of collection of the lens. To get an overall resolution of TEM, spherical aberration, electron lens aberration and chromatic aberration need to be taken into account. Recent advances like aberration-corrected transmission electron microscope has been developed to improve the performance of the TEM.

One of the drawbacks of the TEM technique is that many samples require extensive preparation before doing TEM. Requirements for TEM samples include: be no bigger than sample holder; be electron transparent; have same internal structure (preparation of sample shouldn't change structure of previous sample); be free of artifacts and be clean. There are two kinds of preparation for TEM specimen. One is self-supporting disk and the other is TEM grid[35]. To make a self-supporting disk, the thinning process contains four steps. First is an initial thinning to create a thin slice from a bulk material. Second is cutting a disk from this slice. Prethinning the disk is next. Finally, using methods like electropolishing and ion milling to achieve the required sample thickness. To make a TEM grid, the sample to be characterized is generally a solution or a suspension and is dropped on the grid with a metal loop. After fully drying, particles within the solution or suspension are ready to be imaged.

There are some other limitations of the TEM characterization. For instance TEM can only give 2D images of 3D specimens. Thus other surface-sensitive or depth-sensitive techniques may be necessary to complement the results from TEM. Electron beam damages and safety issues are also big concerns when using TEM instrument.

## 3.2.2 Sample preparation

In our case, to prepare the TEM sample, first, zeolite nanosheets suspension was diluted from the starting concentration. Otherwise, there were too many zeolite particles appeared in one scanning area and it was hard to take diffraction patterns of one single zeolite nanosheet. Then a metal loop was used to transfer the diluted zeolite nanosheets suspension to a TEM grid (ultrathin carbon film on holey carbon support film, 400 mesh Cu, Ted Pella) and the grid was dried in ambient environment. To ensure the drying, the TEM grid was normally left overnight before doing imaging. An FEI Tecnai T12 TEM operating at 120 kV was used for characterization. Both the images of the nanosheets and the diffraction pattern of a single sheet were achieved from the TEM. With the images, the purity of the suspension and the crystallinity of the nanosheets were determined.
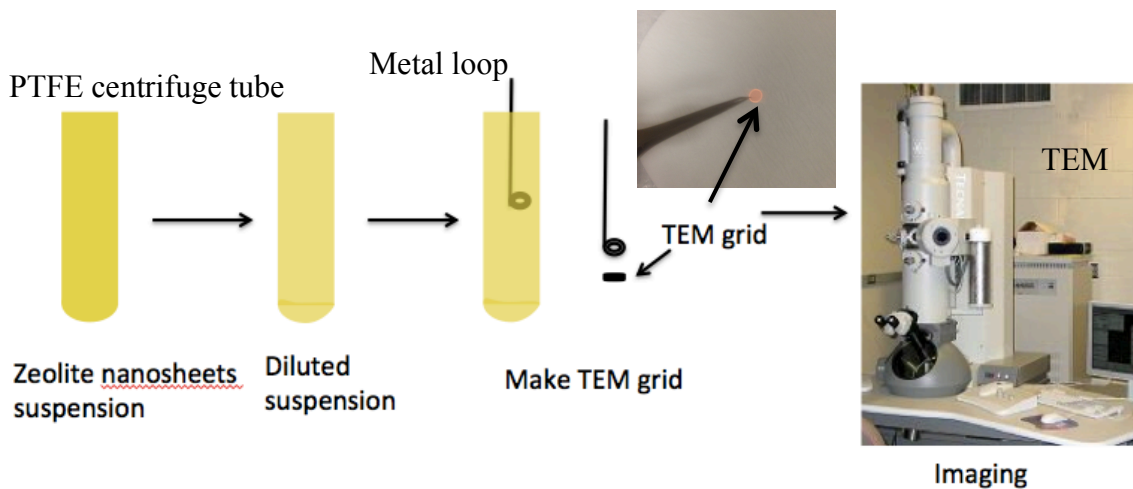
Fig 3.2 Sample preparation procedure for TEM

## 3.3 XRD

### 3.3.1 General description

X-ray diffraction (XRD) was developed to study the structural properties of crystalline and amorphous materials on an atomic scale. It is a non-destructive method that can identify crystalline phases and orientation and determine structural properties like lattice parameters, grain size and preferred orientation. It has wide medical and scientific applications[37, 38].

Normally XRD instrument contains three parts: X-ray source, a goniometer and a detector. The wavelength of X-rays is typically 1-100 angstroms which is the same order of magnitude as the spacing between planes in a crystal. Thus X-rays can be used to produce significant diffraction patterns of a sample. The radiation of the source is considered monochromatic with the wavelength of the highest peak in the spectrum for general calculation of X-ray measurements.

Understanding of X-ray diffraction can be obtained from the Bragg's law[38]. Bragg proposed that the X-rays scattered from adjacent planes would remain in phase if the path-length difference equals an integer number of the X-ray wavelength. The diffraction angle for constructive interference corresponds directly to a certain crystallographic

lattice distance 'd' that is a distinct property for each material. So by slowly varying the incident angle, the spacing information of the sample can be attained and thus determine whether or not the right material has been made.

Bragg's model gives that

$$2dsin\theta = n\lambda$$

Below is the figure that demonstrates the geometrical conditions of Bragg's law:
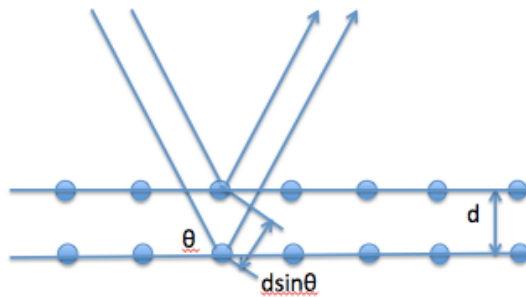


Fig 3.3 Bragg diffraction

A $\theta - 2\theta$ scan method is used in this thesis for both determination of multilammellar MFI zeolite structure and characterization of zeolite nanosheet films orientation. For measuring particle orientation, intensity of the diffraction peaks can be used to represent the degree of alignment.

To get the orientation information of the deposited thin films, both in-plane XRD measurements and out-of-plane measurements are applied. In-plane XRD can be utilized to measure diffraction intensities from lattice planes perpendicular to the surface of the samples[39]. In symmetric out-of-plane XRD measurements, the incident angle is generally large and thus the incident beam travels deeply into the sample. So, for a thin film, the XRD intensity from the film is hard to detect while intensity from the substrate is dominant, which causes trouble for measurements and understanding of the data. This is the reason why in-plane XRD is required for thin film measurements. An in-plane XRD scan normally has a very small incident angle; therefore, the incident beam does not

penetrate far into the sample, permitting effective analysis. Applications of in-plane XRD measurements include characterization of ultra thin films, analysis of structural depth profile, and in-plane orientation evaluations.

(a)

Incident beam        Diffracted beam

(b)

Incident beam

$\theta$

$2\theta$

$\theta$

$2\theta$

$\psi$

Diffracted beam

$\omega, \phi$
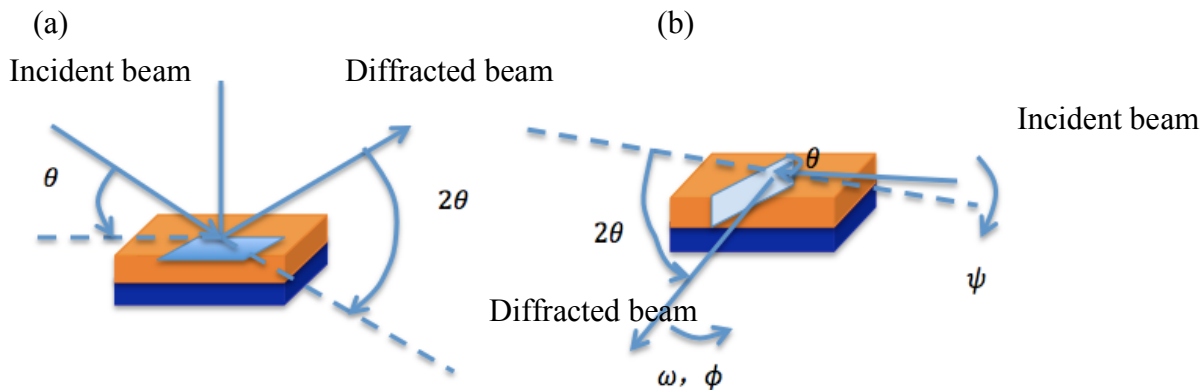
Fig 3.4 (a) Out of plane XRD measurement (b) In-plane XRD measurement

Long-term exposure to X-rays is harmful and leads to severe damages to the body. So most of the X-ray devices used today contain security interlock shutters and automated shut-down procedures of the X-ray source in case of potential exposure. Users need to be aware of the potential danger and safety training is mandatory before using the instrument.

In this work, for multilamellar MFI zeolite, XRD patterns were collected with a Bruker AXS (Siemens) D5005 Wide Angle Diffractometer. For zeolite nanosheets coatings, out of plane XRD data was collected using a Bruker D8 Discover 2D. The aligning laser pinpointed the area to be scanned. It always pointed at the center part of the sample in the experiments by manual control. This instrument used a Cu Ka radiation point source. The 2D detector was applied to collect large amount of data simultaneously. In-plane XRD data was collected by Panalytical X'pert Diffractometer. The X-ray generator was set to 45 kV and 40 mA.
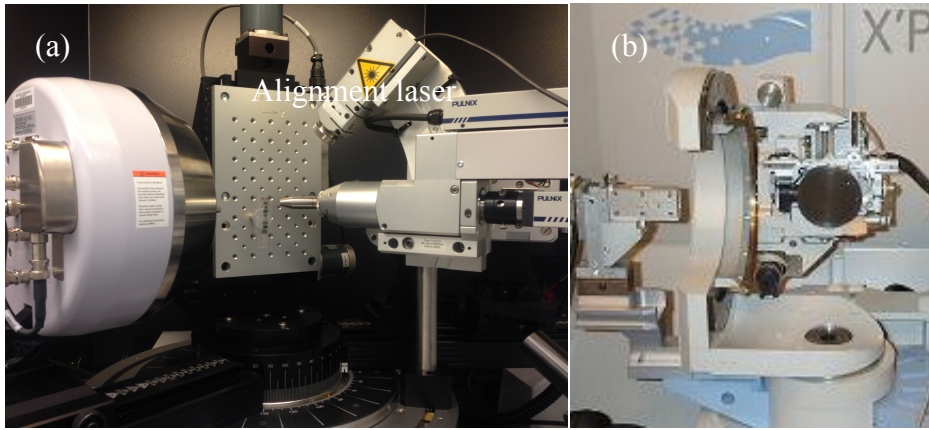
Fig 3.5 (a) Bruker D8 Discover 2D (b) Panalytical X'pert Diffractometer

# 4 Materials

## 4.1 MFI

MFI is a member of high-silica zeolites. It has a unique channel structure that makes it a very important catalysis in the petrochemical industry[1].

### 4.1.1 Structure of synthetic zeolite MFI

MFI has units of 12 T atoms (Si, Al). The T12-units contain two 5-1 units and form left- and right- handed chains along **c** direction. And the left- and right- handed chains can form Periodic Building Unit when related by a mirror plane perpendicular to **b** direction. The neighboring Periodic Building Unit can be connected by a rotation of $180^o$ about **a** direction and a shift of 1/2 **b**. 10-ring channels within the MFI zeolite create cavities. Linkages of the cavities form two kinds of channels. One is a sinusoidal 10-ring channel and the other is a straight channel[40, 41].
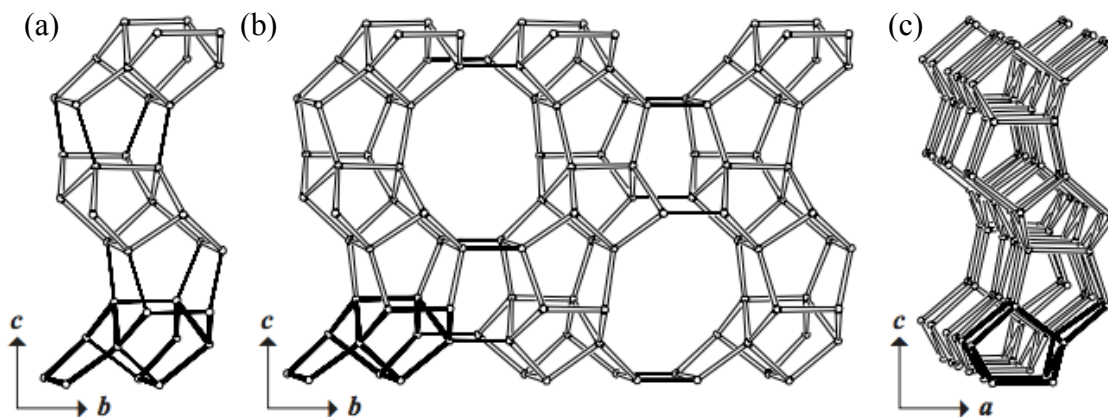


Fig 4.1 (a) Polar chain viewed along **a** direction, (b) Periodic Building Unit viewed along **a** direction and (c) along **b** direction[40]

(a)                          (b)
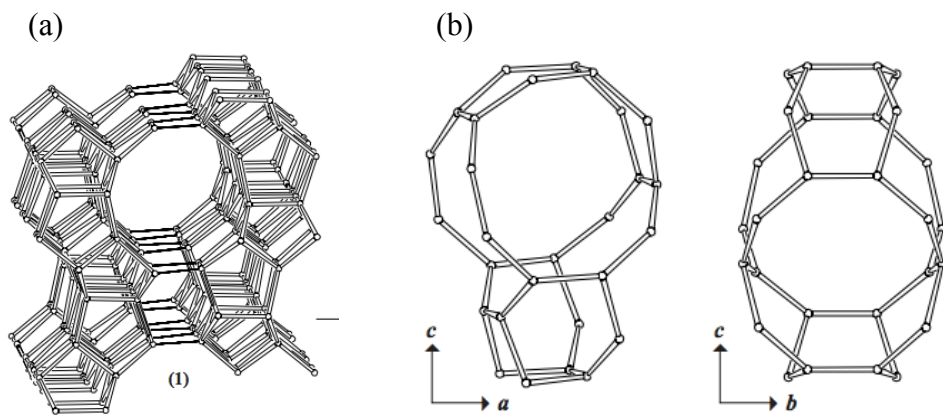


Fig 4.2 (a) Connection mode of MFI (b) MFI cavity [40]

(a)                                    (b)
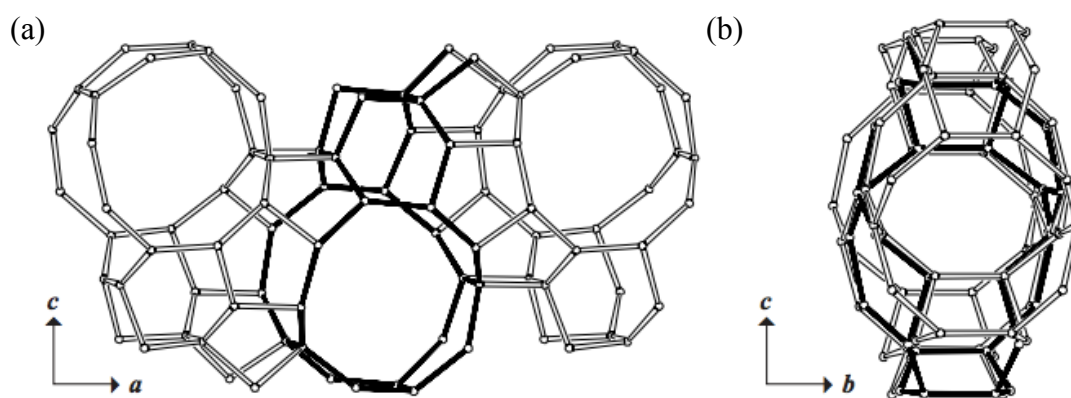


Fig 4.3 Linkage of cavities into sinusoidal 10-ring channels[40]

(a)                                    (b)
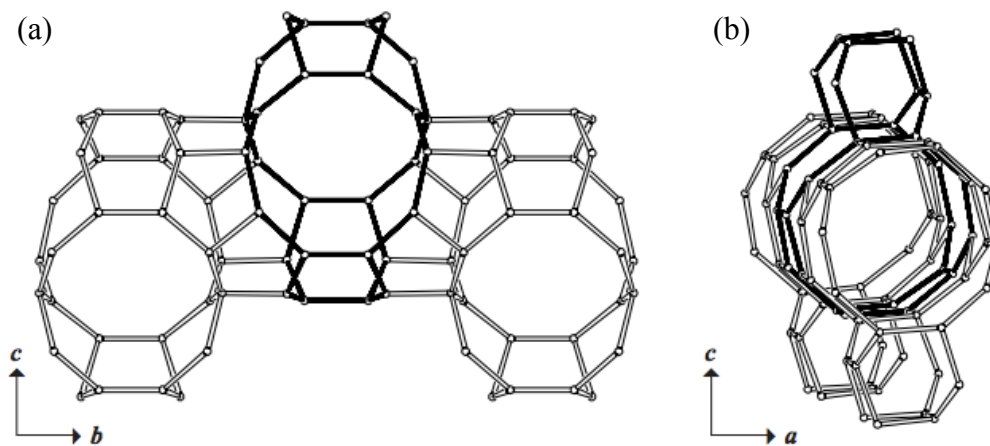


Fig 4.4 Linkage of cavities into straight channels[40]

## 4.2 Making the suspension

In this section, preparation of exfoliated MFI nanosheets suspension in n-octanol is presented.

### 4.2.1 Synthesis of multilamellar MFI

High-aspect-ratio zeolite nanosheets[4] are desirable in terms of making membranes[42], catalysts[43] and nanocomposites[44] for separations. To make multilammellar MFI zeolite nanosheets, Choi et al.[1] designed a diquaternary ammonium-type surfactant. Two positively charged nitrogen atoms in the surfactant direct the MFI framework structure, while the long hydrocarbon chain prevents growth of MFI along its b-axis. This specifically designed surfactant directs the formation of layered MFI nanosheets with an overall thickness of 20-40 nm. In this thesis, this method was applied to synthesize the layered precursor for MFI nanosheets.
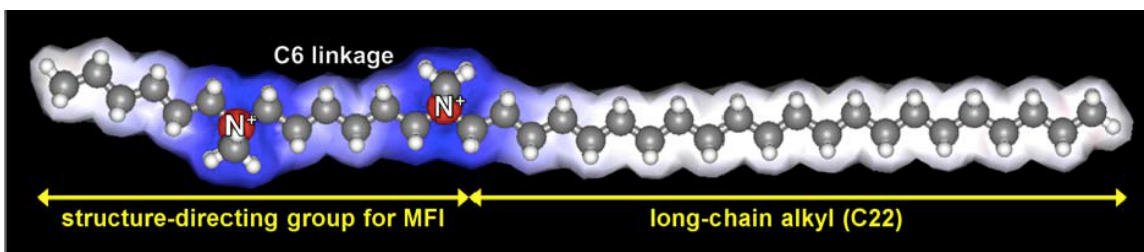


Fig 4.5 Structure of diquaternary ammonium-type surfactant [1]

#### 4.2.1.1 Synthesis of organic structure-directing agent

To synthesize multilamellar MFI, the 'bifunctional' cationic surfactant acting as structure-directing agent was made. The synthesis of the organic structure-directing agent (OSDA) for the layered MFI took place via two reactions. First reaction was the alkylation of a diamine with 1-bromodocosane and the second was alkylation of the product of the first reaction with 1-bromohexane.

In the first reaction, a one-liter round bottom flask with three 24/40 openings, a condenser, two 24/40 caps, a 100 mL glass measuring flask, a magnetic stirrer, a glass sparger, a

sparger cap, a dry tube and a glass funnel were cleaned using soap water, rinsed with deionized water and then dried in the drying oven at 70 ℃. 23.3 g of 1-bromodocosane were added in the flask that was then connected with the condenser. The whole setup was covered with aluminum foil since the reaction is sensitive to light and degased in the vacuum chamber of the glove box. After that, the setup was transferred to the hood containing oil bath. 300 mL acetonitrile, 300 mL toluene and the magnetic stirrer were added. The sparger was connected to argon cylinder and an argon flow rate of 50 mL/min was maintained during the reaction. Stirring was set at a speed of approximately 600 rpm. All connections were ensured to be leak free. The temperature of the oil bath was increased to 70℃. Then 103.2 g of N, N, N', N' tetramethyl, 1-6 diaminohexane was added into the flask via a funnel. The whole reaction ran for 10 hours or longer.

After the reaction, heat was turned off and stirring was stopped. The round bottom flask was raised up to drain out most of the oil and cool down. The cooled product was vacuum filtered by 25 micron cellulose filter papers on a Buchner funnel and then collected in a glass beaker. Diethyl ether was added in the glass beaker to mix with the cake for 10 to 15 minutes. The mixing and the vacuum filtration were repeated for two more times. The cake was then placed in a 500 mL round bottom flask. A rotary evaporator was used to completely dry the product. After the cake was fully dried, the product was stored in the round bottom flask covered with aluminum foil.
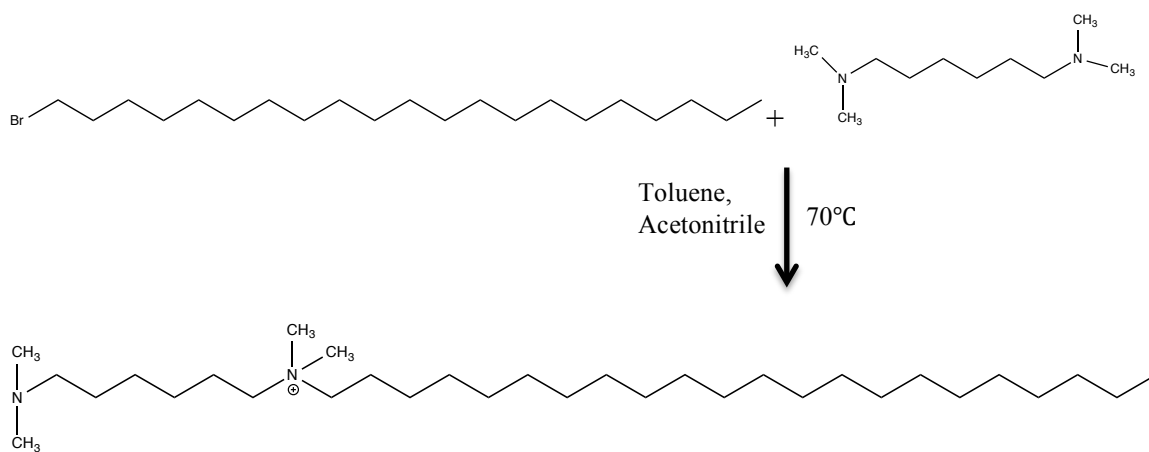
Fig 4.6 Alkylation with 1-bromodocosane

28

In the second reaction, dried product from the first reaction was added in a round bottom flask. The solvent was 600 mL acetonitrile and the temperature of oil bath was set to be 85℃. Other steps were the same as the first reaction. At the final step, stoichiometric amount of 1-bromohexane was added in the flask. The reaction ran for 10 hours or longer. When the reaction was done, the filtration, washing and drying steps as in the first reaction were repeated. NMR was carried out to analysis the structure of the OSDA.
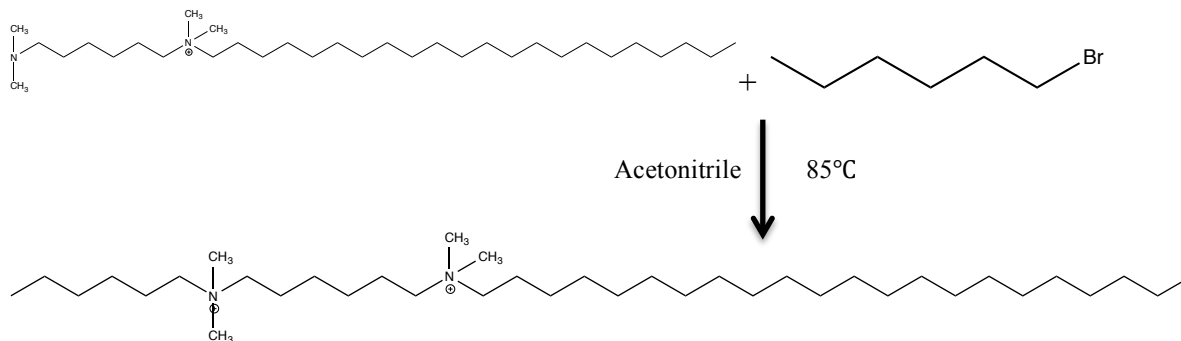


Fig 4.7 Alkylation with 1-bromohexane

The ChemBioDraw program is used to simulate the NMR results for OSDA. Fig 4.8 and 4.9 show simulation and experimental results for $H^1$-NMR shift. The peaks between 1 and 1.5 correspond to H in $-CH_2$ that not near $N^+$. Peaks between 2 and 3 cannot be found in experimental results, while in modeling they come from H in $-CH_2$ and $-CH_3$ that are near $N^+$. Fig 4.10 and 4.11 show simulation and experimental results for $C^{13}$-NMR shift. The images are very alike, indicating experimental result corresponds well with the simulation result.

29
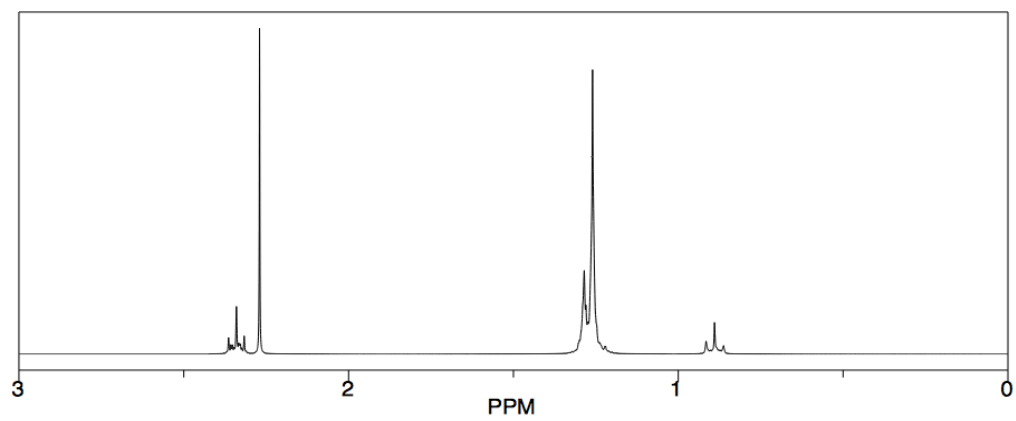
Fig 4.8 Simulation of H$^1$-NMR shift
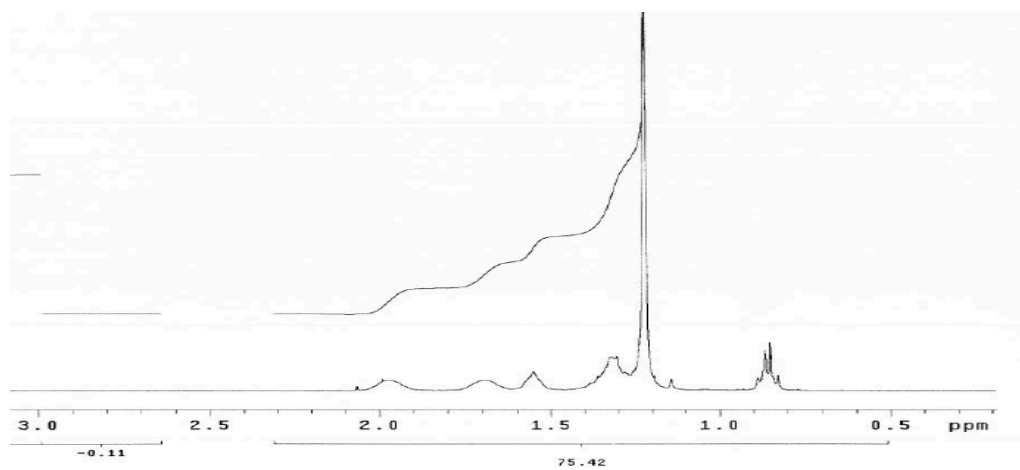


Fig 4.9 Experimental H$^1$-NMR shift
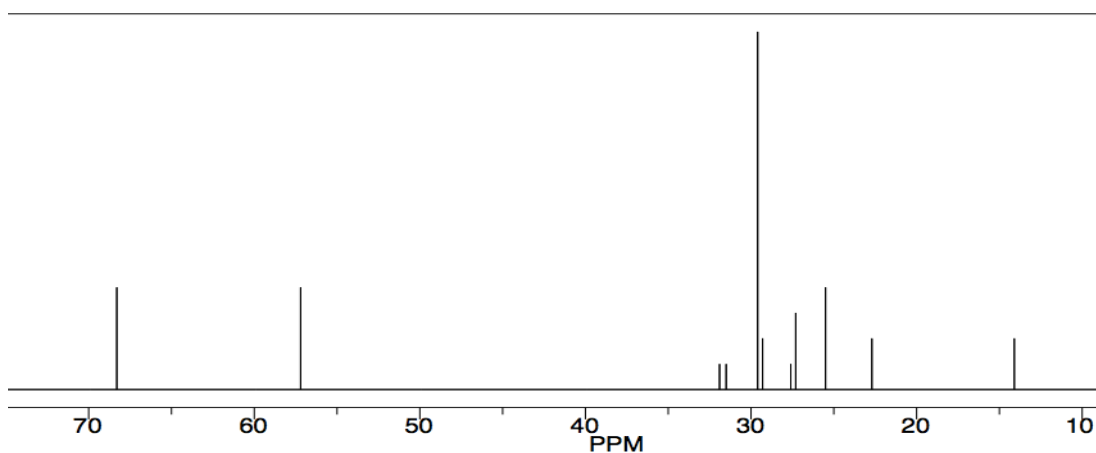
Fig 4.10 Simulation of C$^{13}$-NMR shift
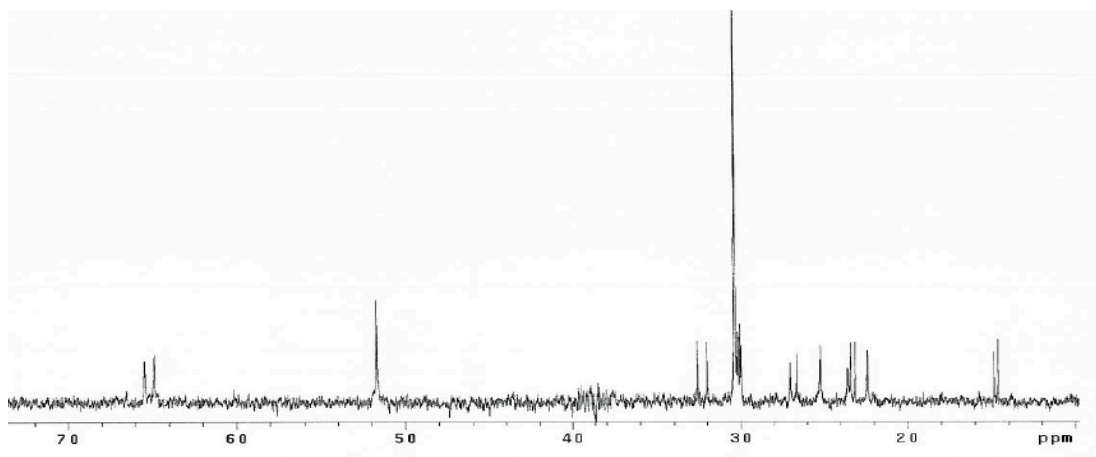


Fig 4.11 Experimental C$^{13}$-NMR shift

### 4.2.1.2 Synthesis of multilamellar MFI

Ion-exchange reaction, hydrolysis reaction and hydrothermal reaction followed to achieve multilamellar MFI. 0.20M aqueous solution of OSDA was made in a polypropylene beaker with 2X (X represents the molarity of OSDA) silver oxide (II) added. The reaction was covered with aluminum foil since it is sensitive to light. The ion-exchange reaction ran for 4 days. After 4 days, the content was vacuum filtered through a 25 micron cellulose filter paper on a Buchner funnel. The filtrate was blackish or brownish and was centrifuged at 40,000 g for 3 hours to sediment excess silver oxide (II). The clear supernatant was stored.

The concentration of the OSDA solution was measured by carrying out titration with 0.1 N HCl solution. The concentration of [OH⁻] was increased until higher than 0.2083M for synthesis of multilamellar MFI. To achieve this concentration, a rotary evaporator was used to evaporate water. This process took 2-4 hours depending on the vacuum level. After the concentration reached the required value, the OSDA solution was stored in a polypropylene or polytetrafluoroethylene (PTFE) container and used within a week.

To synthesize multilamellar MFI, OSDA solution, water and tetraethyl orthosilicate (TEOS) were added into a polypropylene container using the following stoichiometric ratio: 100 TEOS : 15 $(C_{22-6-6})(OH)_2$ : 4000 $H_2O$. After 2 to 3 minutes, the mixture became a gel and stirring slowed down or even stopped. The magnetic stirrer was removed at this point and the gel was mixed using a KitchenAid blender for 1-2 minutes. If the gel consistency did not become thin after the blending, the gel was left in the container for a day. If the gel consistency became thin, the magnetic stirrer was added back and a steady stirring was maintained for 16-24 hours at 600 rpm.

30 g of gel was filled in HF cleaned Teflon liners and the liners were put in a rotation oven preheated at 150℃. A thermometer was added in the oven to measure the temperature and the setting point was adjusted until the thermometer actually read 150℃. The rotation was kept to maximum. The temperature and the autoclaves were checked everyday to ensure a correct temperature and a continuing rotation of autoclaves. After 7-10 days, the autoclaves were taken out, transferred to sink and cooled down with running water. Autoclaves were opened in the fume hood and the liners were taken out. The contents in the liners were transferred to 50 mL PTFE centrifuge tubes and spun down at 5000 g for 10 minutes. The supernatant was discarded. Fresh deionized water was added to mix the contents. A lower G-force was used for next several centrifugations to remove amorphous materials. The centrifugation was repeated until the pH of the suspension fell below 9. The powder product was dried at 130℃ in oven and stored in a quartz vial. It was characterized with XRD, SEM and TEM.

The XRD pattern that shows in Fig 4.12 is similar to that in reference 1. Only h0l reflections are sharp enough for indexing, which corresponds to that the zeolite thickness along *b*-axis is relatively small while *a-c* planes have large coherent domains. This confirms that a material contains high-aspect-ratio zeolite nanosheet is made successfully using this process.

SEM and TEM images shown in Fig 4.13 and 4.14 reveal that the MFI zeolite has a plate-like morphology composed of three-dimensionally intergrown nanosheets as mentioned in Choi's paper[1]. Layered structure can be observed very clearly in the TEM images.
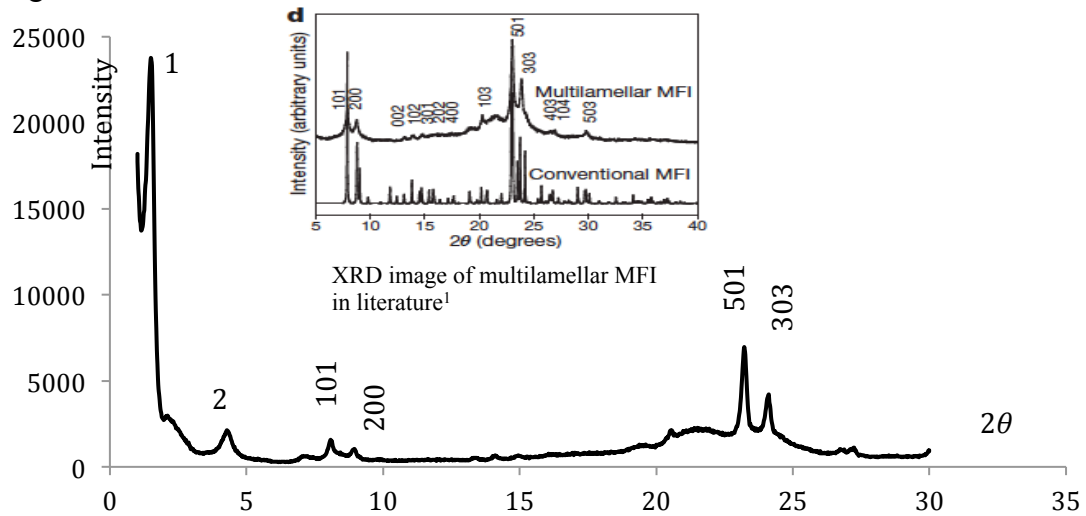


Fig 4.12 XRD image of the multilamellar MFI zeolite

Table 4.1 XRD data of multilamellar MFI

| Peak 1 | d/angstrom | Peak 2 | d/angstrom | hkl(101) | d/angstrom |
|---|---|---|---|---|---|
| | 65.874 | | 21.326 | | 11.126 |
| hkl(200) | d/angstrom | hkl(501) | d/angstrom | hkl(303) | d/angstrom |
| | 10.040 | | 3.850 | | 3.714 |
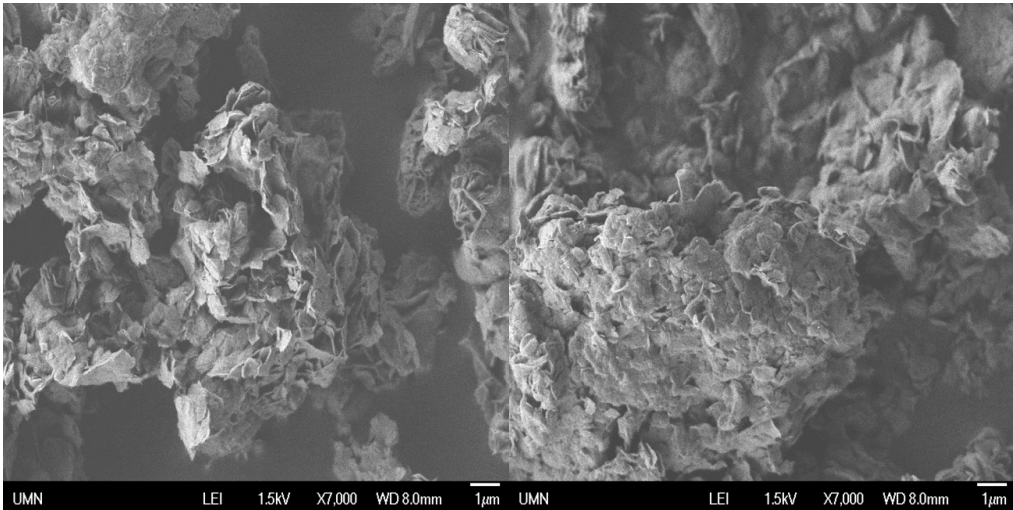
Fig 4.13 SEM images of the multilamellar MFI zeolite
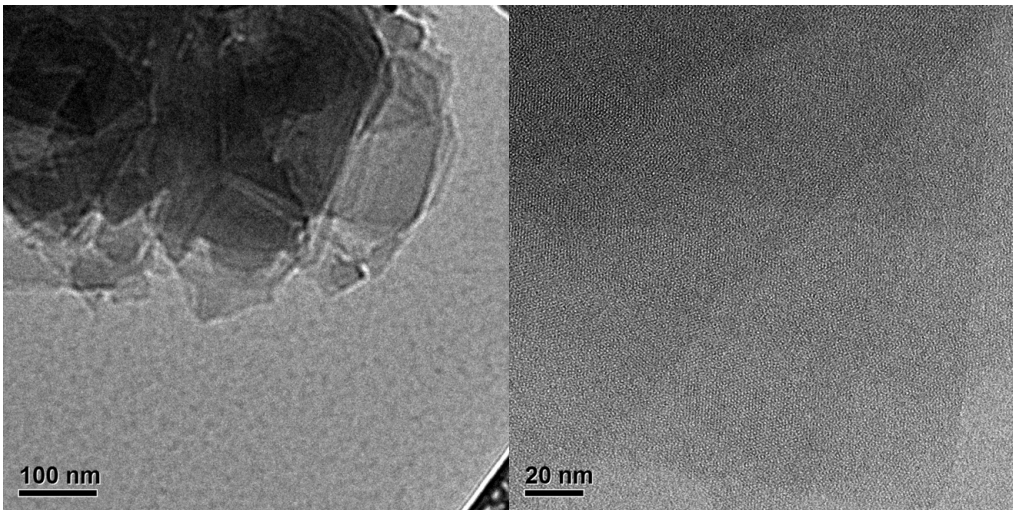


Fig 4.14 TEM images of the multilamellar MFI zeolite taken by Meera Shete, a graduate student in Michael Tsapatsis' group

## 4.2.2 Melt blending

To prepare isolated and intact zeolite nanosheets from multilamellar MFI, exfoliation using melt blending was applied[45]. The melt blending process involves mixing a kind of polymer powder with a stacking of layered materials above the glass transition temperature or melting point of the polymer. During the blending, the polymer chains diffuse from the bulk of the polymer into the galleries between the layers[46, 47]. By careful

34

manipulation of the temperature change during the process, composites of the polymer and the exfoliated materials can be made.

To prepare polymer and zeolite composites, two melt extruders accompanying with two kinds of polystyrene were used in this thesis. One is DACA compounder using higher molecular weight polystyrene (MW=35000) and the other one is DSM melt extruder using polystyrene oligomer (MW=900).

**DACA compounder**

For DACA compounder, in a single run, only 4 g nanocomposites were made. The machine and the screws were ensured to be clean and the die hole was checked to be unblocked. The machine was turned on after the screws were put in place and the chamber was closed. The empty load was increased to above 50 by turning the screw below the extrusion chamber in counter clockwise fashion and recorded. The machine was then heated up to 120℃ by entering the value in the computer connecting to it. Before feeding the material, the lever was ensured pointing inward so that the machine was in recirculation mode. The motor speed was set to 300 rpm and the motor was started. The torque and the time when the motor started were recorded. 4 g of polystyrene (MW=35000) were added for cleaning. Nitrogen flow was switched on immediately after feeding to avoid degradation of polymer. The temperature was increased to 180℃ after feeding polystyrene and the mixing was maintained for 5 minutes. In the meantime, 1 L liquid nitrogen was prepared in a clean large polypropylene beaker and covered with aluminum foil to prevent contamination. After 5 minutes of mixing at 180℃, the motor and nitrogen flow were turned off before opening the chamber. Screws were taken out and put in the liquid nitrogen. Material sticking to extrusion chamber was scrapped off using a wooden spatula. The extruder was cleaned using tissue paper. After cleaning was done, the temperature was reduced to less than 50℃. Polystyrene from the screws was scrapped off wearing protective gloves. After everything was clean, all the above steps were repeated till polymer feeding. A mixture of 3.84 g polystyrene and 0.16 g zeolite was fed this time. Nitrogen flow was switched on immediately after feeding the material

to avoid degradation of polymer. The machine ran at 120°C for 20 minutes, at 170°C for 25 minutes, at 150°C for 30 minutes and at 200°C for 20 minutes sequentially. Exact time was recorded when changing temperatures. After running at 200°C for 20 minutes, the temperature was decreased to 150°C. As soon as it reached 140°C, the lever was turned outward so that melt came out. The screws were kept running until temperature went below and then came back and stabilized at 150°C. By this time, most of the product was out. Another 1 L liquid nitrogen was prepared in a clean large polypropylene beaker and covered with aluminum foil to prevent contamination. The motor and nitrogen flow were turned off. The screws were taken out and put in liquid nitrogen. The set temperature of the machine was then increased to 180°C, making it easier to scrap off material sticking to extrusion chamber using spatula and clean the extruder using tissue paper. After cleaning was done, temperature was reduced to less than 100°C and the machine was turned off. The product was scrapped off from screws and all products were stored in a glass vial.

**DSM extruder**

For DSM extruder, 15 g of zeolite-polystyrene nanocomposites were made in a single run. The air flow valve, the water flow valve and the nitrogen gas cylinder valve connecting to the DSM compounder were opened. Nitrogen flow was adjusted to 50 cc/min. The melt compounder was then turned on and the die temperature was set to 120°C. Screws speed was activated at 250 rpm. The melt compounder was then purged with polystyrene oligomer (Eantman company) to remove the traces of purge polymer left from last experiment. 15 g (MW=900) polystyrene oligomer was fed using the feeder and mixed in the machine for 5 minutes. The discharge valve was opened to remove the polymer. The amount of polymer that came out (weight = x gram) was weighed and (15-x) gram polymer was fed again. This purging was repeated until the oligomer coming out seemed clean. The weight of oligomer coming out after last purging was measured (y gram). The nitrogen flow was closed before feeding 0.6 g zeolite and (14.36-y) gram polystyrene. After feeding completed, the feedhole was closed and nitrogen was turned on again. Zeolite was mixed with polystyrene at 150°C for 20 minutes and exfoliated at 60°C for 30

minutes. After this process, the temperature was increased to 80℃ and the discharge valve was opened to collect the product. The product was stored in a clean container and its weight was measured. After most of the product was out, the temperature was increased to 150℃. The discharge valve was closed and a same amount of purge polymer as the weight of the product was added. After 10 minutes of mixing, the purge polymer was removed. Purging was repeated for several times until the purge polymer coming out appeared clean. The temperature was reduced to 30℃ after the purging. Screws were taken out and all the inner parts of the compounder were cleaned thoroughly with a brush. All the valves were closed after the experiment. Fig 4.15 shows what the nanocomposites look like from the DSM extruder.



Fig 4.15 Nanocomposites of polystyrene and zeolite from DSM extruder

## 4.2.3 Density gradient centrifugation

Polymer and unexfoliated nanosheets from the melt blending process are detrimental for fabricating coatings in later experiments. Polymers removal during heat treatment causes curling and agglomeration of nanosheets. Unexfoliated zeolite leads to packing issues. So a purification method to remove unwanted polymer and unexfoliated zeolite nanosheets is required.

A density gradient centrifugation method is developed by Agrawal et al.[2] to purify exfoliated nanosheets. This method contains a series of centrifugation steps to remove the polymer and unexfoliated nanosheets. Density gradient centrifugation method is

developed based on the fact that particles sediment with different velocities due to density differences. After enough centrifugation time to arrive at equilibrium, particles with the same density gather together in the same density zone. Thus different density particles separate from each other. For particles with different size and shape but same density, a non-equilibrium method is used[48]. In this situation, separation of particles is time dependent, meaning larger particles sediment at a faster rate comparing with smaller particles.

### 4.2.3.1 Removal of polystyrene

For polystyrene removal, density of polystyrene is 1.06 $g/cm^3$ while density of denser zeolite nanosheets are about 2 $g/cm^3$. A two-fraction density gradient is created with bottom liquid being a poor solvent of polystyrene and having a density between polystyrene and the zeolite nanosheets. In this way, polystyrene cannot diffuse into the bottom solvent while zeolite nanosheets are able to sediment and deposit at the bottom of the centrifuge tube, separating zeolite nanosheets from polymer[2].

Due to different molecular weight of polystyrene, nanocomposites made from DACA compounder and DSM extruder followed different procedures for polystyrene removal. All solvents used in this process were filtered (0.2 micron PTFE syringe filter) in the clean hood to remove contaminations previously exist in the solvents. PTFE centrifuge tubes (Fisher Scientific) were used for high G-force centrifugation. Before using, all centrifuge tubes were cleaned with soap water, rinsed with deionized water, ethanol and filtered solvents.

### Removal of polystyrene with molecular weight 35000

For nanocomposites produced by DACA, 3 g of nanocomposites were dispersed in 300 g of filtered toluene to make 1% suspension in a 500 mL conical flask. Eight 50 mL PTFE centrifuge tubes were prepared with sealing cap assembly for centrifugation. The sealing cap was ensured to have Viton o-ring. The o-rings, centrifuge tubes and the caps were inspected for any visible damage. All centrifuge tubes were filled to the neck with the

suspension and balanced with counter weight. Their weight difference was less than 0.1 g. The centrifuge rotor (JA 25.50) was checked for any visible damage before the tubes were put in. The temperature was set to -1℃, the centrifugal force was set to 12,000 g and the time was set to 3 hours. The centrifugal force was increased to 40,000 g after temperature reached -1℃ and when the temperature became steady after increasing centrifugal force, it was changed to 4℃. The tubes were taken out gently at the end of the run without shaking the cake and transferred to the fume hood. Supernatant was shaken
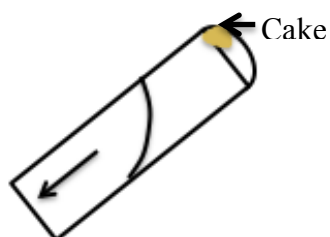


Fig 4.16 Discard supernatant

off and discarded without losing the cake as shown in Fig 4.16. The sedimented zeolite nanosheets were redispersed in fresh toluene and all suspensions were transferred to a single tube. All the other tubes were rinsed with filtered toluene and transferred again to that single tube. If the cake was not completely dispersed, a maximum 2-3 minutes of bath sonication (Branson 5510R-DTH, 135 watts) was used. The suspension in this single tube was centrifuged again at 40,000 g for 3 hours. The resulting cake was then redispersed in 20 mL fresh toluene. 20 mL chlorobenzene was filled in a cleaned centrifuge tube. 1 mL toluene was placed on top of the chlorobenzene, drop by drop by a transfer pipette. The tip of the pipette was close to the liquid surface in the centrifuge tube as shown in Fig 4.17. The suspension of nanosheets was then placed on top of the 1 mL toluene the same way. The centrifuge tube was filled up to the neck. If not, fresh toluene was added to make up the level.



Fig 4.17 Way to add another solvent to create density gradient

Centrifugation was carried out at 40,000 g for 3 hours. The two-fraction density gradient centrifugation was repeated twice. At the end of the third run, the sedimented nanosheets were collected by pouring out the supernatant and redispersed in n-octanol. After washing nanosheets in n-octanol by carrying out another centrifugation at 40,000 g for 3 hours, the sediment was redispersed in 20 mL fresh n-octanol by horn sonication (Qsonica Q500, 500watts, 0.125" micro-tip operating at 20% of maximum amplitude).

To use the horn sonicator, its tip was cleaned using ethanol wipe. A stop pulse of 5 seconds for every 20 seconds of sonication was set to avoid overheating. Horn sonication was carried out for 3 minutes. At this point, most of the polymer (MW=35000) was removed. The suspension was characterized with TEM.

**Removal of polystyrene oligomer with molecular weight 900**

For nanocomposites produced by DSM, instead of chlorobenzene, dichloromethane was used and due to low molecular weight polystyrene, only one time density gradient centrifugation was enough for polymer removal. 3 g melt compounding nanocomposites were equally added in four 50 mL PTFE centrifuge tubes each containing 20 mL toluene. The nanocomposites were dispersed by vortex. The tubes were centrifuged at 40,000 g for 3 hours. Supernatant was discarded and the cakes were redispersed in toluene and transferred to one single tube. All the other tubes were rinsed with toluene and transferred again to that single tube. Toluene was added to fill that tube to top and the cake was dispersed using vortex. This one tube was centrifuged with its counterbalance at 40,000 g for 3 hours. The nanosheet sediment was again redispersed in 20 mL fresh toluene using vortex. 20 mL dichloromethane was added in a clean tube. 1 mL toluene was placed slowly on top of the dichloromethane, drop by drop using a transfer pipette and the 20 mL toluene suspension was placed on top of the 1 mL toluene the same way. After making this density gradient, centrifugation was carried out at 40,000 g for 3 hours. The sediment was dispersed in n-octanol this time. After washing nanosheets in n-octanol by carrying out another centrifugation at 40,000 g for 3 hours, the sediment was redispersed in 20 mL fresh n-octanol. The suspension was then characterized with TEM.

Fig 4.18 (a) shows the suspension with polystyrene (MW=35000) in it. The spheres in the image are polystyrene. Fig 4.18 (b) is taken from suspension after polymer removal. There are no spheres in the image, only large unexfoliated zeolite particles and exfoliated zeolite nanosheets with lighter contrast. This suspension is qualified for the next step centrifugation.
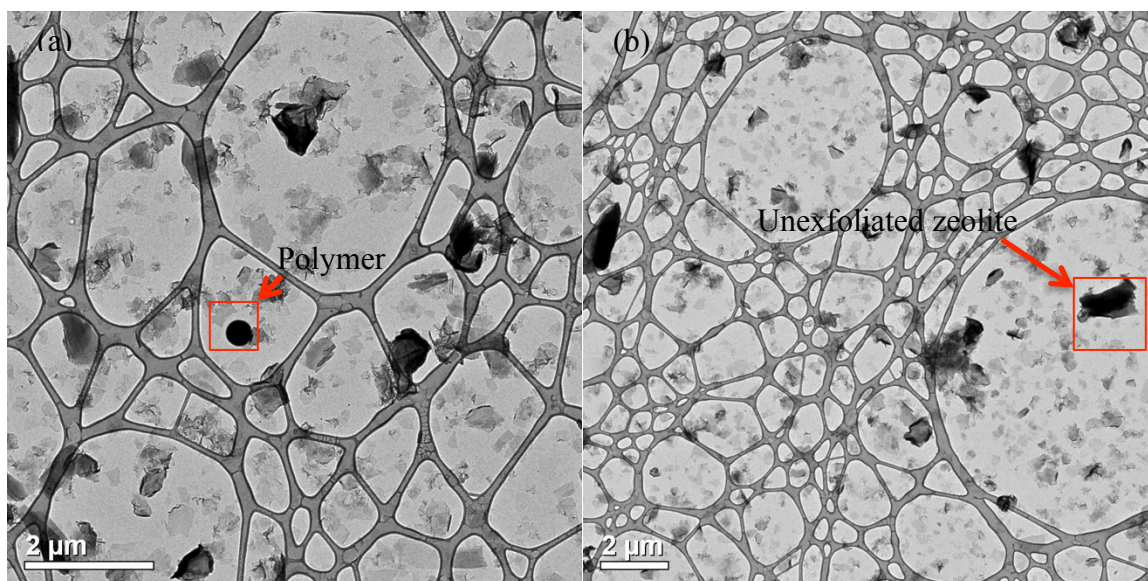
Fig 4.18 TEM images of MFI nanosheets after removing polystyrene (MW=35000) taken by Meera Shete (a) With polymer, the spheres in the image are polystyrene (b) No polymer

### 4.2.3.2 Removal of unexfoliated zeolite nanosheets

The next step of density gradient centrifugation is removal of large unexfoliated zeolite nanosheets. Exfoliated nanosheets have the same density as unexfoliated nanosheets. However, due to size and shape differences, they can be separated based on differences in sedimentation rate[2].

To make the density gradient, 5 mL, 5 mL, 10 mL and 10 mL water were added sequentially in a clean centrifuge tube and each volume was marked. Then in later steps, different solvents were added to the marks. A nonlinear multilayered density gradient was created in a 50 mL PTFE centrifuge tube by sequentially placing 5 mL chloroform, 5 mL dichloromethane, 10 mL chlorobenzene, and finally 20 mL nanosheet suspension in octanol prepared from polymer removal. In old procedure, centrifugation was carried out at 12,000 g for 30 minutes at room temperature. In new procedure, to remove unexfoliated zeolite nanosheets more efficiently, centrifugation was carried out at 20,000 g for 30 minutes. At the end of centrifugation, half of top fraction (10 mL) was collected

in a clean tube. The bottom fractions were also stored. The collected top fraction was diluted to 40 mL and centrifuged at 40,000 g for 3 hours. The sediment was redispersed in n-octanol using vortex. After washing nanosheets in n-octanol by carrying out another centrifugation at 40,000 g for 3 hours, the sediment was dispersed in a known volume of n-octanol. Its concentration was measured and it was characterized with TEM.

Fig 4.19 (a) is the TEM image taken from suspension after unexfoliated zeolite nanosheets removal. It shows that only exfoliated zeolite nanosheets can be found, indicating a complete removal of both polymer and unexfoliated zeolite particles in this suspension. The uniform contrast from isolated nanosheets suggests uniform thickness. There are also particles presenting in (a) appear as coils with dark contrast. They are agglomerate particles and may cause packing issue for later films fabrication. Due to low ratio of these agglomerate particles comparing with flat, segregated zeolite nanosheets, this batch of suspension is still considered as suitable for coating experiments. The diffraction pattern in Fig 4.19 (b) is the same as electron diffraction pattern of MFI nanosheets down their b-axis, proving that nanosheets are still MFI crystalline after the density gradient centrifugation purification process.
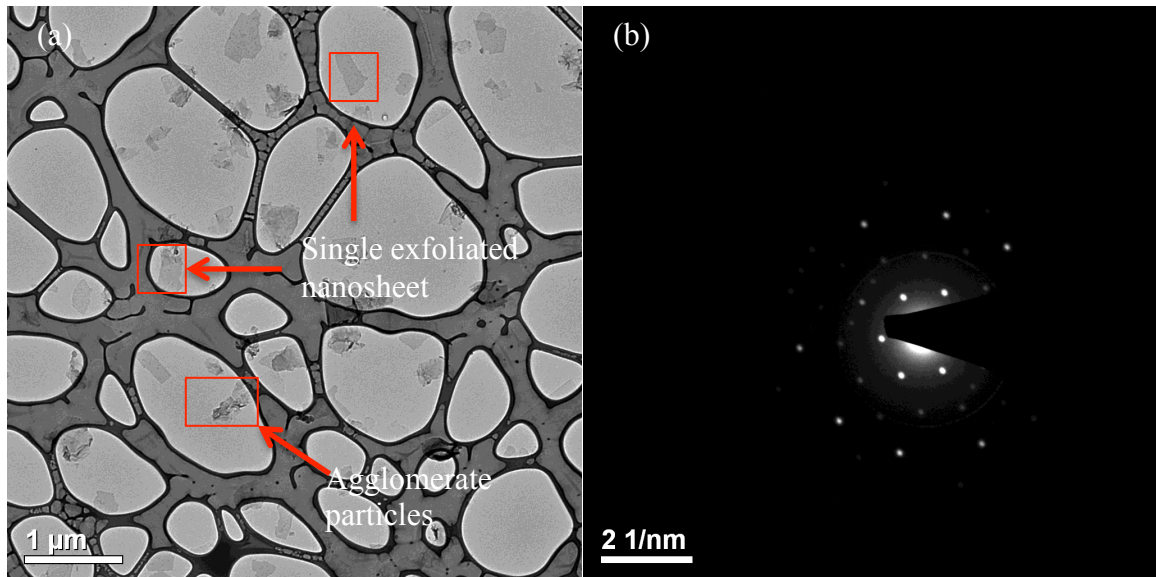


Fig 4.19 TEM images of MFI nanosheets after removing unexfoliated zeolite nanosheets taken by Meera Shete

42

## 4.3 Yield of exfoliated zeolite nanosheets

The yield of nanosheets after one melt blending process and a cycle of density gradient centrifugation can be calculated after qualified suspensions as shown in Fig 4.19 were made. The yield calculated here is for exfoliated zeolite nanosheets made from DACA and purified from higher molecular weight polystyrene (MW=35000). About 1 g of the qualified suspension was coated on an alumina support. The nanosheets film was then coated with about 300 nm Au by a sputter coater to protect it from beam damages from the focused ion beam (FIB). FIB (Quanta 3D DualBeam) was used to create the cross-section of the film. Scanning electron microscope images of the cross-section were taken using JEOL 6700 operating at 1.5 kV and tilting to 40-48°. As presented in Fig 4.20, zeolite film is the thin film between alumina support and protective Au film.
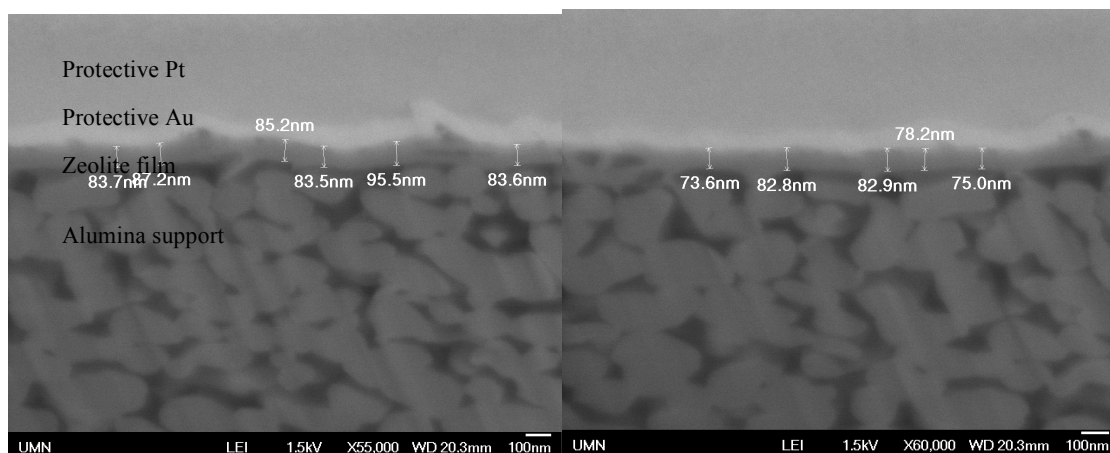


Fig 4.20 SEM images of the cross-section prepared by FIB

The radius of the alumina support is 11mm. Assuming packing density of the coating is 0.8, volume of nanosheets in coating is $V = A$ (area of the alumina support) $\times$ T (thickness of the coating) $\times 0.8 = 2.61 \times 10^{-11} \ m^3$. Density of zeolite nanosheets is assumed to be 2 g/cm$^3$. Then mass of nanosheets in coating is $M = V \times 2 = 5.21 \times 10^{-5}$ g. So the concentration of the exfoliate zeolite nanosheets made for calibration is $C = 5.21 \times 10^{-5}/(5.21 \times 10^{-5} + 1) = 0.0521$wt%. For this batch exfoliated zeolite nanosheets suspension, total amount of exfoliated zeolite particles is 27.2129 g (weight of total

43

suspension) $\times$ C = 0.00141 g. The amount of zeolite has been used is 3 g $\times$ 4 % $\times$ 0.6 = 0.072 g. So the yield is $\frac{0.00141}{0.072} \times 100\% = 1.96$wt%.

For the DACA compounder, normally the yield of zeolite nanosheets after compounding and one cycle of density gradient centrifugation is about 10%. The low yield in this thesis is probably attributed to a waste of zeolite nanosheets during the centrifugation when some zeolite nanosheets are discarded with supernatant. Currently, for the DSM extruder, a higher yield of 16% can be achieved due to lower molecular weight polystyrene. During melt blending, lower molecular weight polystyrene allow exfoliation to happen at a lower temperature than high molecular weight polystyrene. Therefore, viscosity of the mixture can be higher leading to a larger shearing during extrusion. More zeolite can be exfoliated and thus improve the yield. For further yield improvement, recycling of exfoliated zeolite nanosheets in the bottom fractions from the four-fraction density gradient centrifugation can be applied.

In later coating experiments, for the drop coating, four batches of exfoliated zeolite nanosheets produced from the DACA compounder were combined with 2 mL n-octanol added to make the zeolite nanosheets suspension. Bath sonication was applied to ensure a complete dispersion of zeolite nanosheets. As calculated, amount of one batch exfoliated zeolite particles is 0.00141 g. The total weight of the nanosheets used here hence is 0.00141 $\times$ 4 = 0.00564 g. The total weight of the solvent is 2 mL $\times$ 0.824 g/mL = 1.648 g. So the concentration of the suspension is $\frac{0.00564}{1.648} \times 100\% = 0.34\%$.

For the spin coating, exfoliated zeolite nanosheets were made from the DSM extruder. Assumption is made that they share the same yield as those made from the DACA compounder. 2 mL n-octanol was added to four batches combined exfoliated zeolite nanosheets. The concentration of the suspensions for later coating is also 0.34%.

# 5 Coatings

This section will explore the use of both a drop coating and spin coating method to coat the zeolite nanosheets to non-porous substrates. To characterize the coatings, both an optical (light) microscope and a scanning electron microscope were used. Out of plane and in-plane XRD were utilized to achieve orientation information.

## 5.1 Modify the substrate

Hydrofluoric acid is aqueous solution of hydrogen fluoride (HF). It is a colorless solution that is highly corrosive. Based on its material safety data sheet, potential health hazards caused by HF contain server burns to all parts of human body, hypocalcemia (depletion of calcium in the body) and other toxic effects that may be fatal. Therefore, complete protection is required when dealing with HF solution.



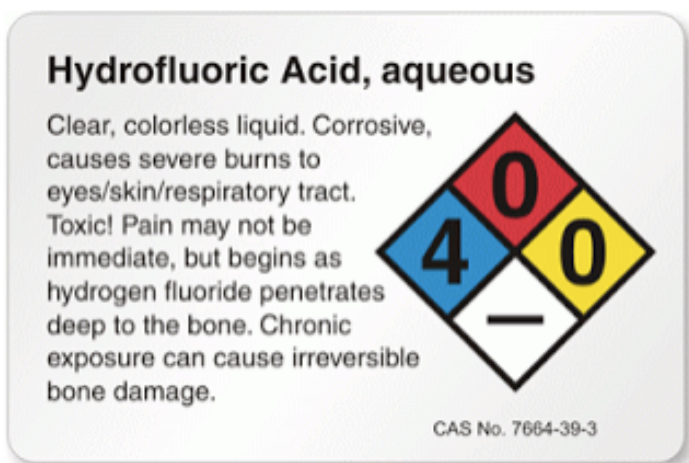Fig 5.1 Emergency overview of HF solution[49]

For routine product use, a hydrofluoric acid-resistant jacket, boots and heavy neoprene or nitrile rubber gloves should be worn for skin protection. A hard hat, chemical safety goggles and a full-face plastic shield is necessary for eye protection. Meanwhile, work should be done in a properly working fume hood when using HF solution to avoid exposure to HF gas.

One-inch silicon wafers were used as the substrates. As mentioned in chapter 2.2.2, the substrates have to be modified to be hydrophobic before coating. The silicon wafer was immersed in distilled water and sonicated for 30 minutes and then be taken to the Minnesota Nano Center at the University of Minnesota and immersed in HF solution for 5 minutes[50] in the wet bench. As HF solution was washed off the substrate using distilled water, the degree of water wettability was observed to ensure the hydrophobicity of the substrate. If water spread on the wafer easily, the wafer was immersed into HF solution again for a few minutes. The hydrophobic wafer was kept in distilled water before making the coatings and was used within 30 minutes after HF etching.

## 5.2 Drop coating

The volume of suspension delivered on the substrate is dependent on the size of the substrate. Too much suspension added causes the liquid to flow off the substrate before drying starts. After determining the appropriate amount of liquids to be deposited, 400 $\mu$L 0.34% exfoliated zeolite nanosheets suspension made as mentioned in chapter 4.3 was dispersed on the modified one-inch silicon wafers (University wafer, Type: N, Orient: (100), Polish: single side polished, Thickness: 380 microns) using a micropipette (Eppendorf Reference, 100 $\mu$L-1000 $\mu$L). After the coatings were fully dried, they were heated to 550℃ to remove OSDA[1, 51]. The calcination was performed under air flow with a 150 mL/min flow rate.
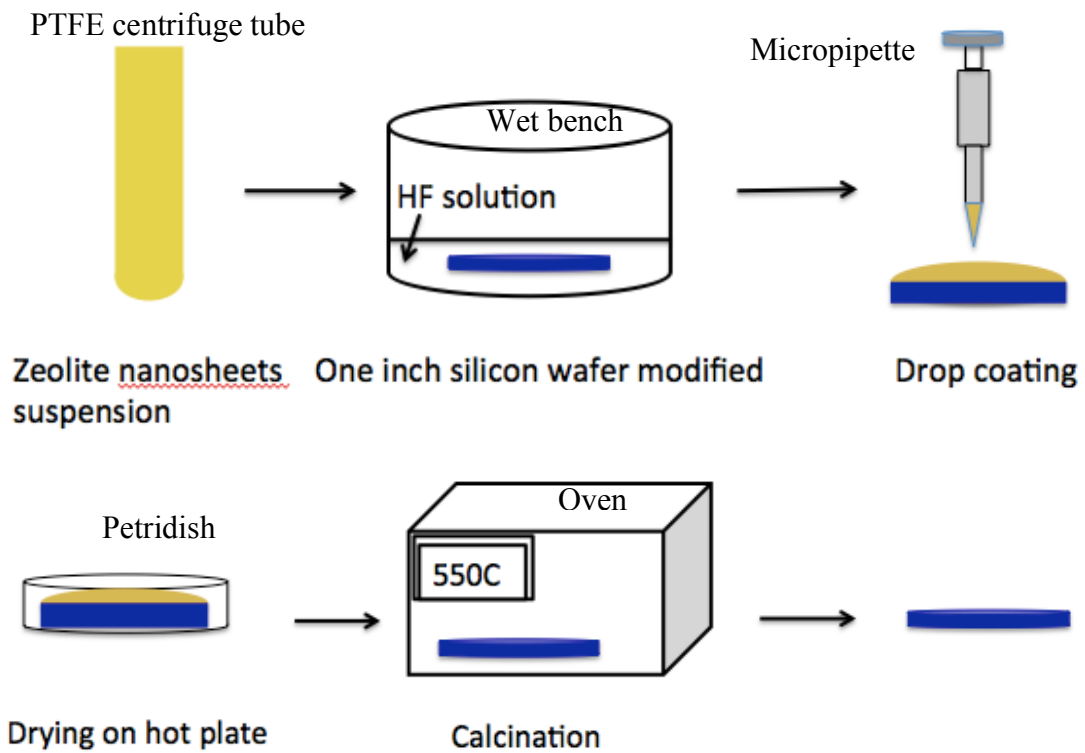
Fig 5.2 Schematic illustration of the process of drop coating

## 5.2.1 Thickness calculation

In this section, an estimation of dry film thickness is given.

For silicon wafer D = 1 inch = 25.4 mm

$$A = \frac{1}{4}\pi D^2 = 5.07 \ cm^2 \tag{5.1}$$

If disperse V = 400 $\mu$L suspension on the wafer

$$h_0 = \frac{V}{A} = 0.0788 \ cm = 788 \ \mu m \tag{5.2}$$

Substitute (5.2) into (2.14)

$$h_{dry} = 788 \ \mu m \times 0.34\% \times 0.414 = 1.109 \ \mu m \tag{5.3}$$

## 5.2.2 Influence of drying temperature

### 5.2.2.1 Optical microscope images

Optical micrographs of coatings dried at 50℃ are shown in Fig 5.3 (a) and (b). Clear color contrasts are shown in the images. Coatings dried at 32.5℃ are shown in Fig 5.3 (c) and (d). Compared to the coatings dried at 50℃, the coatings dried at a lower temperature have a more uniform appearance.
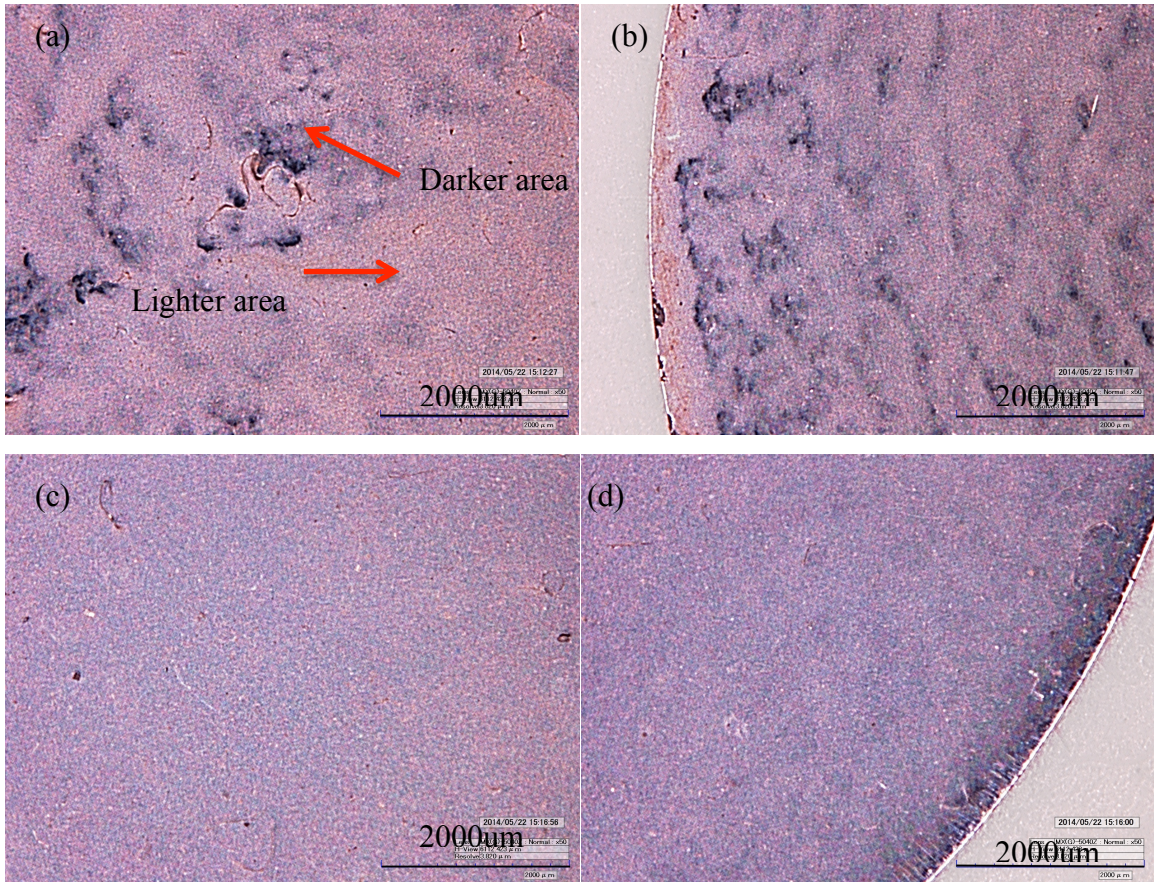


Fig 5.3 Optical microscopy images of (a) center area of the coating dried at 50℃ (b) edge area of the coating at 50℃ (c) center area of the coating at 32.5℃ (d) edge area of the coating at 32.5℃

Differences in the appearance result from surface roughness. The light reflection from the sample varies when the surface structure of the film is not uniform. If light emitted from the optical microscope comes from right above the sample, a silicon wafer without coating appears black in optical microscope images. For areas having particles, however, light reflects differently and the appearance is brighter. Areas with less particles show

more silicon wafer and appear to be darker, while areas with more particles are brighter. Therefore, the clear color contrasts indicate surface structure variations at both the center area and the edge area for coatings dried at 50℃. Compared to the coatings dried at 50℃, the coatings dried at a lower temperature have a more uniform appearance, suggesting smaller thickness variations in the coating.

Two hypotheses are brought up to explain this result. First is, during drying, concentration gradients can appear in the coatings as solvent evaporates and the liquid free surface moves down to press the particles. Lower temperature, meaning smaller evaporation rate and longer drying time, may have a more uniform distribution of particles within the wet film. Increased evaporation rate due to higher temperature, however, does not allow enough time for elimination of concentration gradients in spite of the higher diffusion coefficient at high temperature. Therefore, the coating can have a rougher appearance. The second hypothesis is related to aggregation. As drying temperature increases, zeolite nanosheets experience more Brownian motion and will be more likely to interact with each other. Aggregation of particles is more likely leading to the appearance of clusters of particles. Experiments to follow the effect of temperature and particle concentration on aggregation rate would be useful to determine if this hypothesis is correct.

### 5.2.2.2 SEM images

Fig 5.4 and 5.5 show SEM images of these two coatings dried at different temperatures. From high-magnification SEM images for center areas Fig 5.4 (b) and Fig 5.5 (b), the zeolite nanosheets are observed to be more or less oriented along their b-axis with a small amount of particles protruding out of the plane. The entire substrate is fully covered. From low-magnification images Fig 5.4 (a) and Fig 5.5 (a), more tilted zeolite nanosheets can be easily noticed. Edge effect due to capillary flow is also observable from SEM images.

Unlike optical microscope images, within which distinct thickness variation differences between the two coatings dried under different temperatures are revealed, SEM images are very similar for both coatings. This indicates that the drying temperatures used in this experiment only determine large-scale non-uniformities.
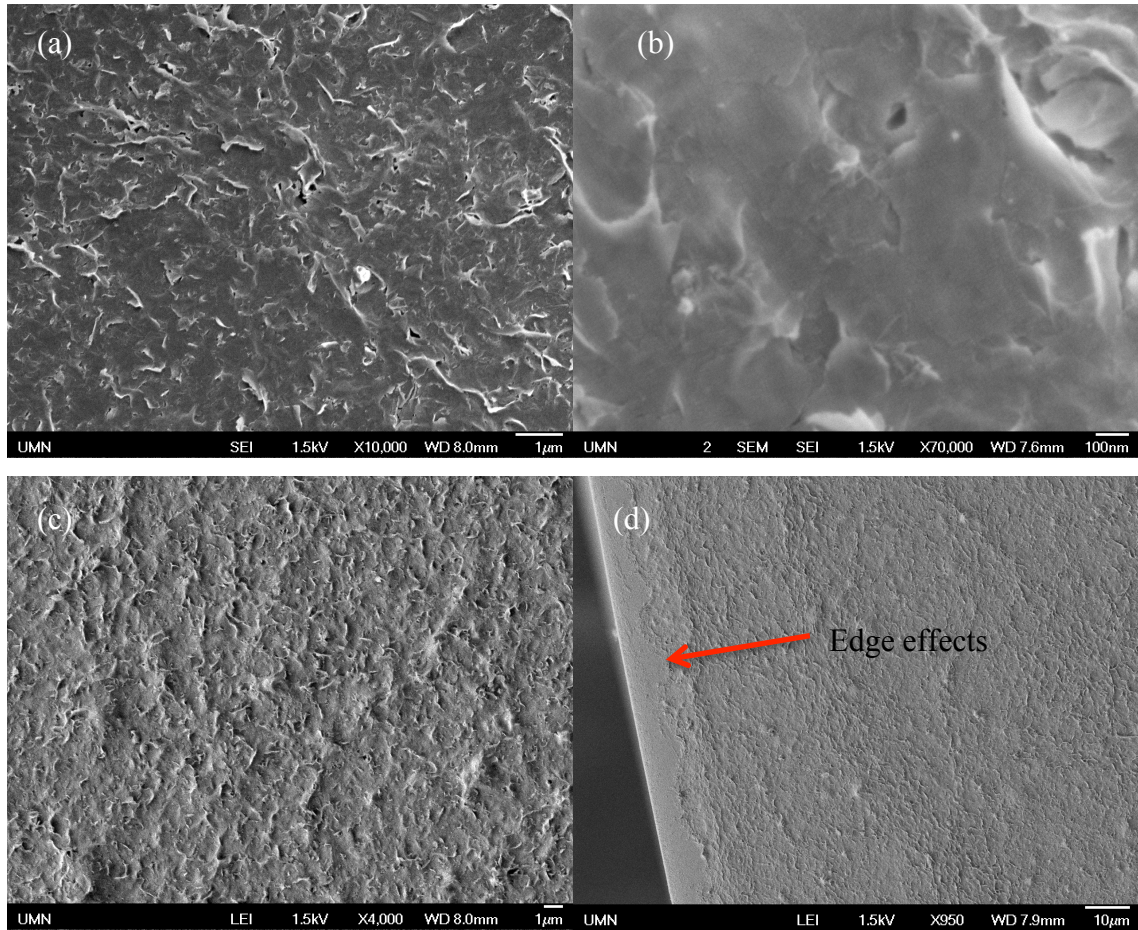


Fig 5.4 SEM images of (a) and (b) center area with different magnifications (c) along radius area (d) edge area for coating dried at 50℃
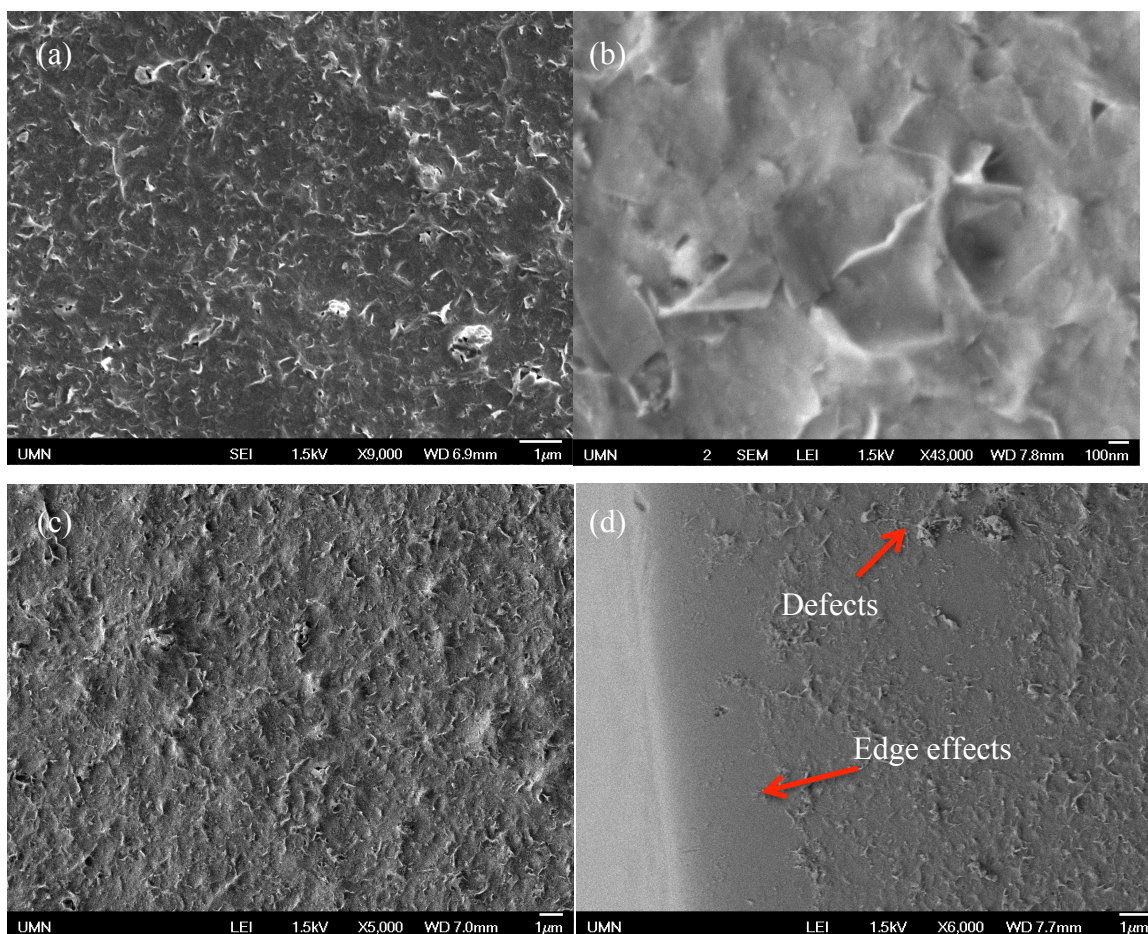
Fig 5.5 SEM images of (a) and (b) center area with different magnifications (c) along radius area (d) edge area for coating dried at 32.5℃

The tilted zeolite nanosheets in both high-magnification images and low-magnification images may be attributed to a few agglomerated particles or curling of larger nanosheets during deposition[2]. From Fig 4.19, agglomerated zeolite particles can be seen. Larger agglomerates sediment quickly to the substrate. When subsequent zeolite nanosheets sediment, they cannot orient themselves parallel to the substrate. This variation in orientation increases as more particles sediment and film thickness increases. Moreover, the MFI zeolite nanosheets are different in shapes and sizes as shown in Fig 4.19, because they are fractured due to exfoliation procedure or vigorous sonication of zeolite sediments when redispersing them in organic solvents during purification step. Non-uniformity of the nanosheets in lateral size can also lower packing efficiency.

51

Furthermore, zeolite nanosheets are so small and thin that disalignment effects like rotational Brownian motion cannot be neglected during drying process.

### 5.2.3 Out of plane XRD data

Fig 5.6 shows out of plane XRD pattern for drop coating films dried at 32.5℃ and 50℃. Out of plane XRD data for a thin film usually comes from lattice planes parallel to the planar substrate. From this image, however, maybe due to too small thickness of the film or spacing variation between layers of nanosheets, the peaks cannot be interpreted as the d-spacing of planes along b direction. This out of plane XRD measurements can be applied for secondary growth films because of larger crystal size and film thickness. Therefore, after secondary growth, out of plane XRD measurements can be taken again for orientation determination. The $2\theta$ angles for peak 1 and 2 are presented in the first two lines of Table 5.1.
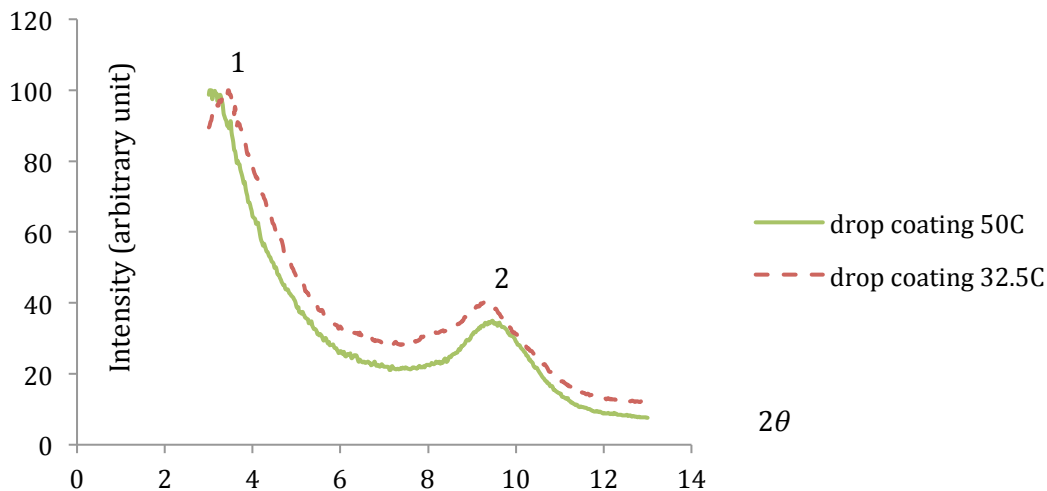
Fig 5.6 Out of plane XRD data of drop coatings

### 5.2.4 In-plane XRD data

Fig 5.7 shows in-plane XRD pattern for drop coating films dried at 32.5℃ and 50℃. The $2\theta$ angles for the (h0l) peaks are presented in the bottom two lines of Table 5.1. In-plane XRD data measures diffraction intensities from lattice planes perpendicular to the planar

substrate. The d-spacing for the peak at 23° is 3.81 angstrom, corresponding to plane (501); while the d-spacing for the peak at 24° is 3.67 angstrom, corresponding to plane (303). Because of the limitation of the instrument, it is very hard to measure low angle peaks ($2\theta$ less than 15 degrees) that can be interpreted as planes parallel to the sample.
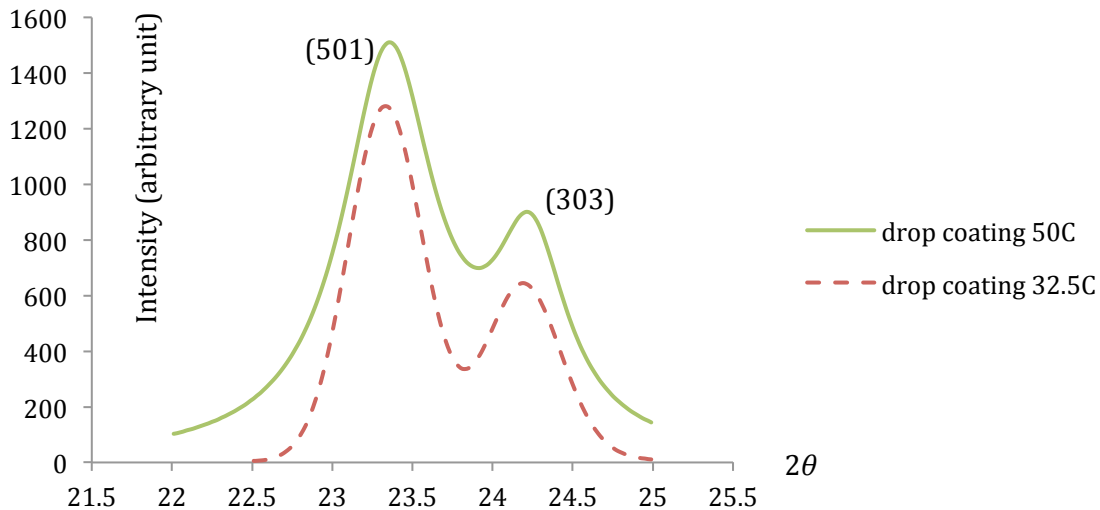


Fig 5.7 In-plane XRD data of drop coatings

Table 5.1 Out of plane and in-plane XRD data of drop coatings

| Out of plane | d spacing of Peak 1/angstrom | d spacing of Peak 2/angstrom |
|---|---|---|
| 50 °C | 3.02 | 9.46 |
| 32.5 °C | 3.46 | 9.28 |
| In-plane | d spacing of hkl (501) /angstrom | d spacing of hkl (303) /angstrom |
| 50 °C | 23.35 | 24.21 |
| 32.5 °C | 23.33 | 24.19 |

53

## 5.3 Spin coating

100 $\mu$L zeolite nanosheets suspension with the concentration 0.34% (see chapter 4.3) was deposited on the modified one-inch silicon wafer (Silicon Inc., Type: N, Orient: (100), Polish: single side polished, Thickness: ~281 microns) using a micropipette (Eppendorf Reference, 100 $\mu$L-1000 $\mu$L). Two different spin conditions were chosen: 1000 rpm for 1 minutes and 500 rpm for 30 seconds. After spin coating, the silicon wafer was transferred to a glass petridish on a hot plate. A thermometer was used to adjust the setting temperature. As measured, for coating made at 1000rpm, the drying temperature is 34.8°C. For coating made at 500rpm, the drying temperature was 31.8°C. The temperature difference is very small and can be neglected during later discussion. After the coatings are fully dried, they were calcined to remove OSDA. Calcination process is the same as mentioned in the drop coating experiment.
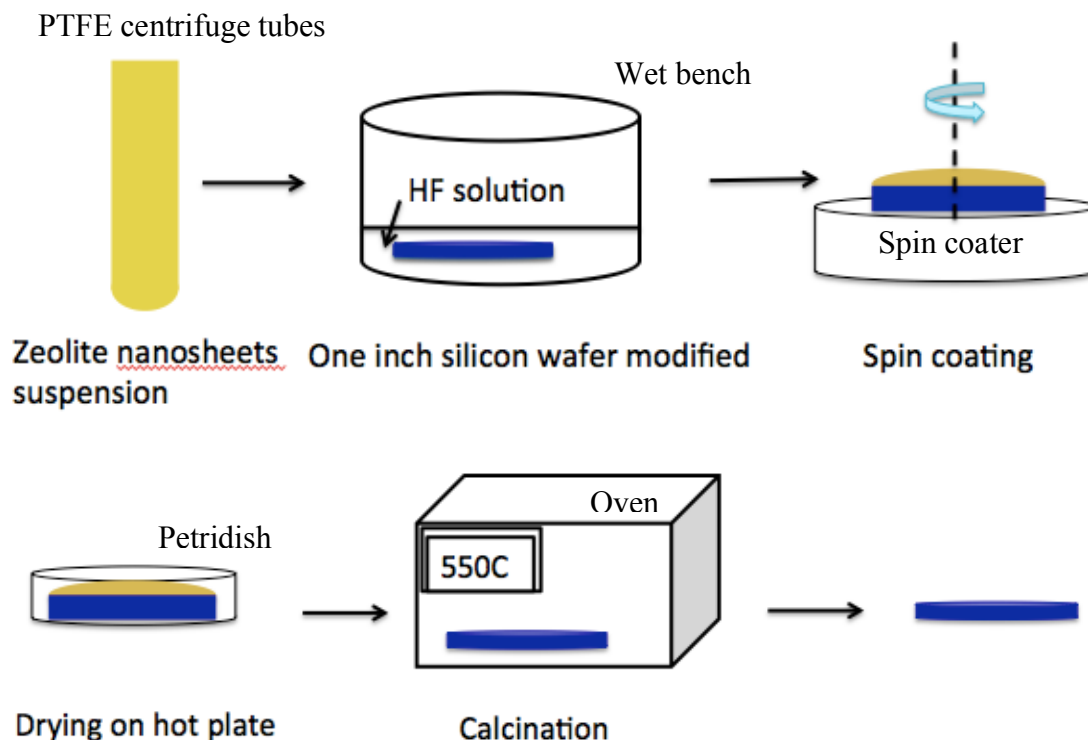
Fig 5.8 Schematic illustration of the process of spin coating

## 5.3.1 Thickness prediction

In this section, mathematic model built in chapter 2 is applied for dry film thickness prediction.

To predict the final film thickness, for silicon wafer D = 1 inch = 25.4 mm

$$A = \frac{1}{4}\pi D^2 = 5.07 cm^2$$

If disperse V = 100 $\mu$L suspension on the wafer, the starting wet film thickness would be

$$h_0 = \frac{V}{A} = 0.0197\ cm = 197.35\ \mu m \tag{5.4}$$

Table 5.2 Properties of octanol

| Density/kg/m$^3$ | 827 | Viscosity/$Pa \cdot s$ | 0.08609 |
|---|---|---|---|

When spin rate = 1000 rpm, angular velocity would be

$$w = \frac{2\pi \cdot 1000}{60} = 104.72\ rad.\,per\ sec \tag{5.5}$$

From Chapter 2,

$$h_{wet} = \frac{1}{\sqrt{\frac{1}{h_0^2} + \frac{4\rho\omega^2}{3\eta}t}} \tag{2.7}$$

Substitute (5.4), (5.5) and physical properties from table 5.2 into equation (2.7), wet film thickness vs. time graph for 1000 rpm spin rate looks like below:



Fig 5.9 Thickness variation vs. time for 1000 rpm spin rate

After 1 minute

$$h_{wet} = 3.44 \ \mu m \tag{5.5}$$

Substituting (5.5) into (2.14)

$$h_{dry} = 4.85 \text{ nm} \tag{5.6}$$

When spin rate = 500 rpm

$$w = \frac{2\pi \cdot 500}{60} = \ 52.36 \ rad.\,per \ sec \tag{5.7}$$

Substituting (5.4), (5.7) and physical properties from table 5.2 into equation (2.7), wet film thickness vs. time graph looks like below:
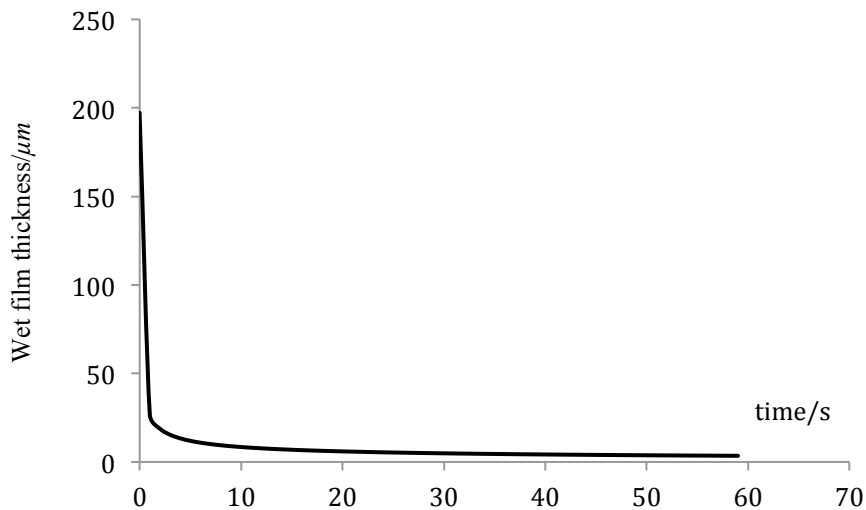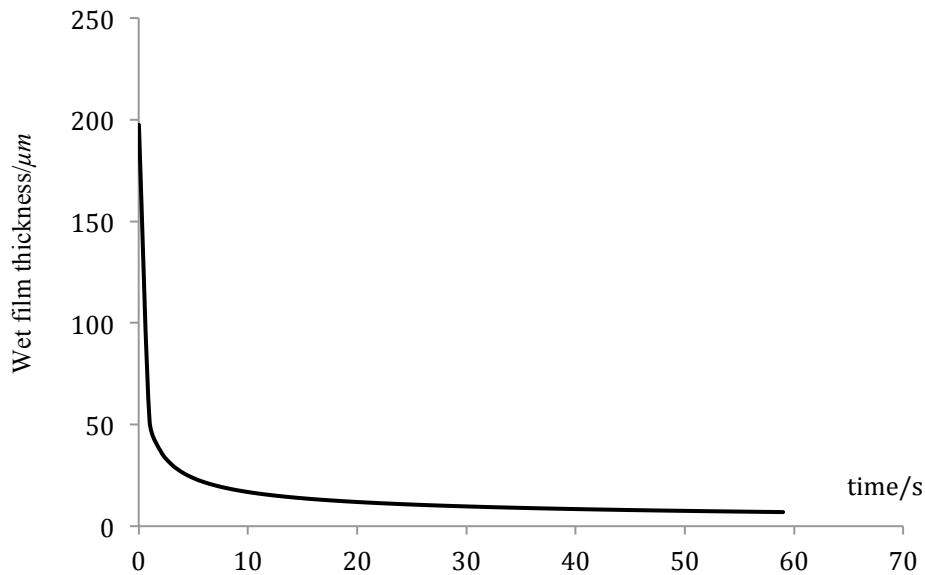


Fig 5.10 Thickness variation vs. time for 500 rpm spin rate

After 30 seconds

$$h_{wet} = 9.73 \ \mu m \tag{5.8}$$

Substituting (5.8) into (2.14)

$$h_{dry} = 13.69 \text{ nm} \tag{5.9}$$

Based on this prediction, thin zeolite nanosheets films can be made within a very short time using spin coating method.

## 5.3.2 Influence of spin rates

### 5.3.2.1 Optical microscope images

For coatings made under the two spin conditions, optical micrographs are shown in Fig 5.11. For high spin rate coating, from Fig 5.11 (a) and (b), the film is more or less uniform with only a little differences in appearance. For low spin rate coating however, from Fig 5.10 (c) and (d), the color contrast appears around a larger area.
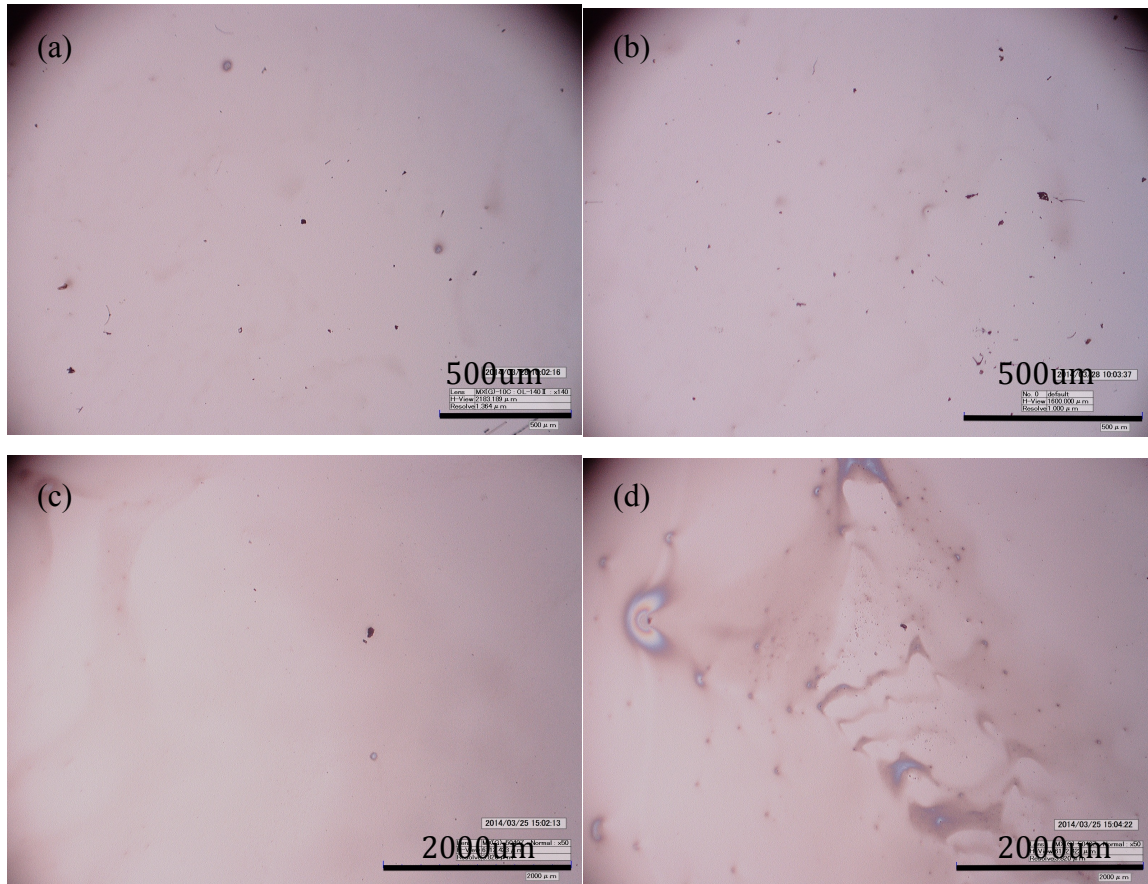


Fig 5.11 Optical microscope images of (a) and (b) center area and along radius area of coating made at 1000 rpm (c) and (d) center area and along radius area of coating made at 500 rpm

More appearance differences indicate thickness variation occupies a larger space of the film. The images look much different than coatings in drop coating, because the light source of the optical microscope was set to shine on the sample from a tilting angle. If

light source comes right above the coatings, due to the small thickness of the spin coating films, optical microscope images for the coatings are almost black showing the appearance of silicon wafers.

The lower spin rate films occupy a larger non-uniform area may be explained by an edge effect observed during the spin coating process. During the spin-off stage, liquid flows outward radially and the film starts to thin. Outflow liquid accumulates temporarily at the edge of the substrate in the form of swellings until droplets form and fly off[12]. The liquid becomes fence-like during the spinning. Only inner area of the film thins uniformly. As the spinning stops, the pinned liquid flows inward from the edge and create non-uniform areas. When the same amount of suspension is delivered on the substrate, for a lower spin rate, larger amount of the liquid is maintained at the edge because of smaller centrifugal force and therefore a larger non-uniform area is produced.
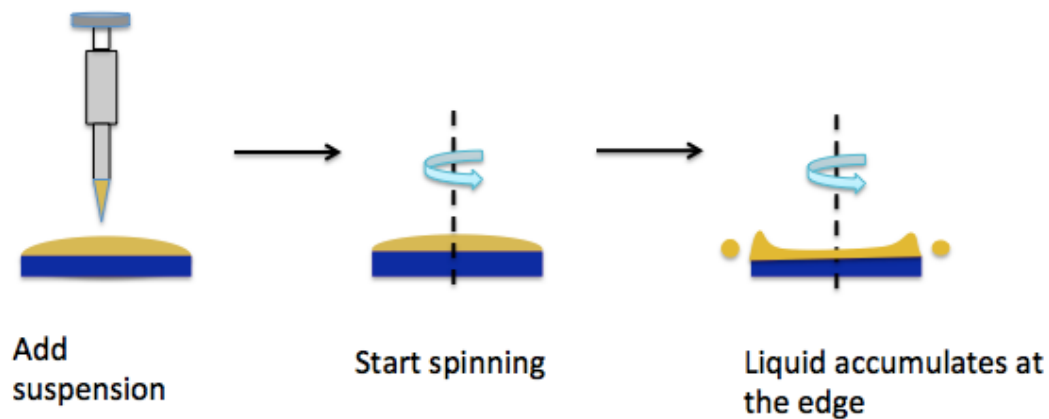


Fig 5.12 Schematic illustration of edge effects during spin coating

Fig 5.13 shows optical microscope images of spin coatings near the edge area. Obvious defects can be detected. This corresponds with the previous explaination about non-uniform area around the edge.
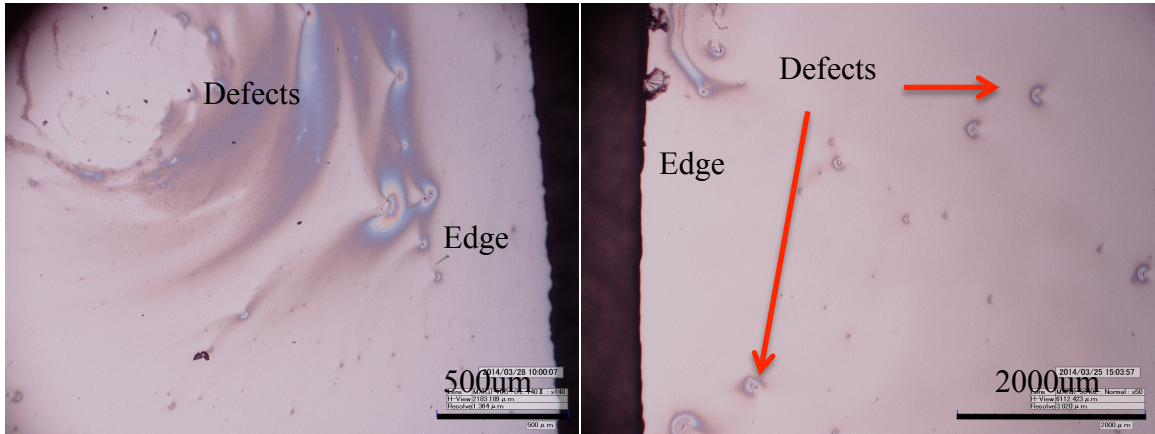
Fig 5.13 Optical microscope images of (a) edge area of coating made at 1000 rpm (b) edge area of coating made at 500 rpm

**Mapping for uniform areas**

Optical microscope images have also been used to map the uniform area of the 1000 rpm and 500 rpm coatings. The uniform area is the small circle excluede the shaded area.

**Mapping for the 1000 rpm coating**

$D_1$ represents the diameter of the large circle, while $D_2$ represent the diameter of the small circle. $A_{arc}$ represents the area of the circular sector ABC. $A_{tri}$ represents the area of triangle ABC. The shaded area can be calculated from a deduction of triangle ABC from circular sector ABC. The arrow pointing from the edge of the large circle to the straight line of shaded area has a length of 5.3 mm.
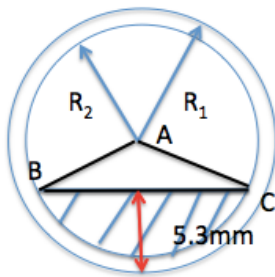


$$D_1 = 1\ inch = 25.4\ mm$$

$$D_2 = 25.4 - 2.5 \times 2 = 20.4\ mm$$

$$A_1 = \frac{1}{4}\pi D_1^2 = 506.71\ mm^2$$

$$A_2 = \frac{1}{4}\pi D_2^2 = 325.85\ mm^2$$

$$A_{arc} = 78.97\ mm^2 \quad A_{tri} = 51.95\ mm^2$$

$$A_{shaded} = A_{arc} - A_{tri} = 27.02\ mm^2$$

$$A_{unifrom} = A_2 - A_{shaded} = 299.83\ mm^2$$

$$\frac{A_{unifrom}}{A_1} = \frac{299.83}{506.71} \times 100\% = 59.2\%$$

**Mapping for the 500rpm coating**

$D_1$ represents the diameter of the large circle, while $D_2$ represent the diameter of the small circle. $A_{arc}$ represents the area of the circular sector ABC. $A_{tri}$ represents the area of triangle ABC. The shaded area can be calculated from a deduction of triangle ABC from circular sector ABC. The arrow pointing from the edge of the large circle to the straight line of shaded area has a length of 10 mm.
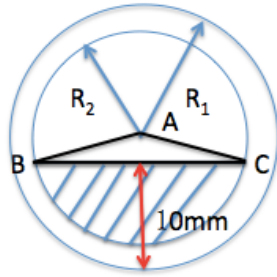


$$D_1 = 1 \; inch = 25.4 \; mm$$

$$D_2 = 25.4 - 5.5 \times 2 = 14.4 \; mm$$

$$A_1 = \frac{1}{4} \pi D_1^2 = 506.71 \; mm^2$$

$$A_2 = \frac{1}{4} \pi D_2^2 = 162.86 \; mm^2$$

$$A_{arc} = 67.54 mm^2 \quad A_{tri} = 26.56 \; mm^2$$

$$A_{shaded} = A_{arc} - A_{tri} = 40.98 \; mm^2$$

$$A_{unifrom} = A_2 - A_{shaded} = 121.88 \; mm^2$$

$$\frac{A_{unifrom}}{A_1} = \frac{121.88}{506.71} \times 100\% = 24.1\%$$

From the mapping, the proportion of uniform area of the higher spin rate coating is almost twice as the lower spin rate coating. However, even with a higher spin rate, 40% of the coating area is still not uniform.

**5.3.2.2 SEM images**

**Center areas**

Fig 5.14 (a), (b), (c) and (d) show SEM images from the center areas for these two spin rate coatings. From low-magnification images (a) and (c), the coverage of the two coatings is uniform around the center area. From high-magnification images (b) and (d), zeolite nanosheets are observed to orient themselves along their b-axis. Meanwhile,

interparticle gaps can be noticed within the higher spin rate coating. The high-magnification images of lower spin rate coating on the other hand, shows that the substrate is fully covered without voids.



Fig 5.14 SEM images of (a) and (b) center area with different magnifications for 1000 rpm coating (c) and (d) center area with different magnifications for 500 rpm coating

A higher spin rate produces a thinner film. Based on prediction of film thickness, spinning at 1000 rpm for 1 minute, the thickness of final dry film should be 4.85 nm. A MFI nanosheet synthesized here usually has a thickness of 3.40 nm, which means the 1000 rpm spin rate film is almost a monolayer film. The model to predict the final film thickness assumes that the entire film thins uniformly, which as discussed before, is not true around the edge. Disturbance caused by inward flow after spinning stops, particles agglomeration and capillary flow are all possible reasons for the interparticle gaps

appearance. For films made at 500 rpm for 30 seconds, the predicted dry film thickness is 13.69 nm, equivalent to about 4 layers of MFI nanosheets. On this condition, a continuous, uniform film is possible to fabricate in the center area. If verification of the actual films thickness is required, the same method as yield measurement can be used. Focused ion beam can be applied for creating cross-section on the films. SEM images of the cross-section can be taken with a tilting angle of the sample stage. If the films thickness is too thin for SEM to measure accurately, TEM may be applied instead.

**Along radius areas**

Fig 5.15 (a), (b), (c) and (d) show SEM images from the along radius areas for these two spin rate coatings. The images are very similar to the ones taken around center area. Low-magnification images (a) and (c) reveal a uniform coverage of the coatings, and high-magnification images (b) and (d) show that zeolite nanosheets are oriented parallel to the substrate with only a few particles curving up. The only difference is interparticle gaps can not only be noticed within the higher spin rate coating but also start to appear within lower spin rate coating, indicating images taken here probably coming from the non-uniform zone.
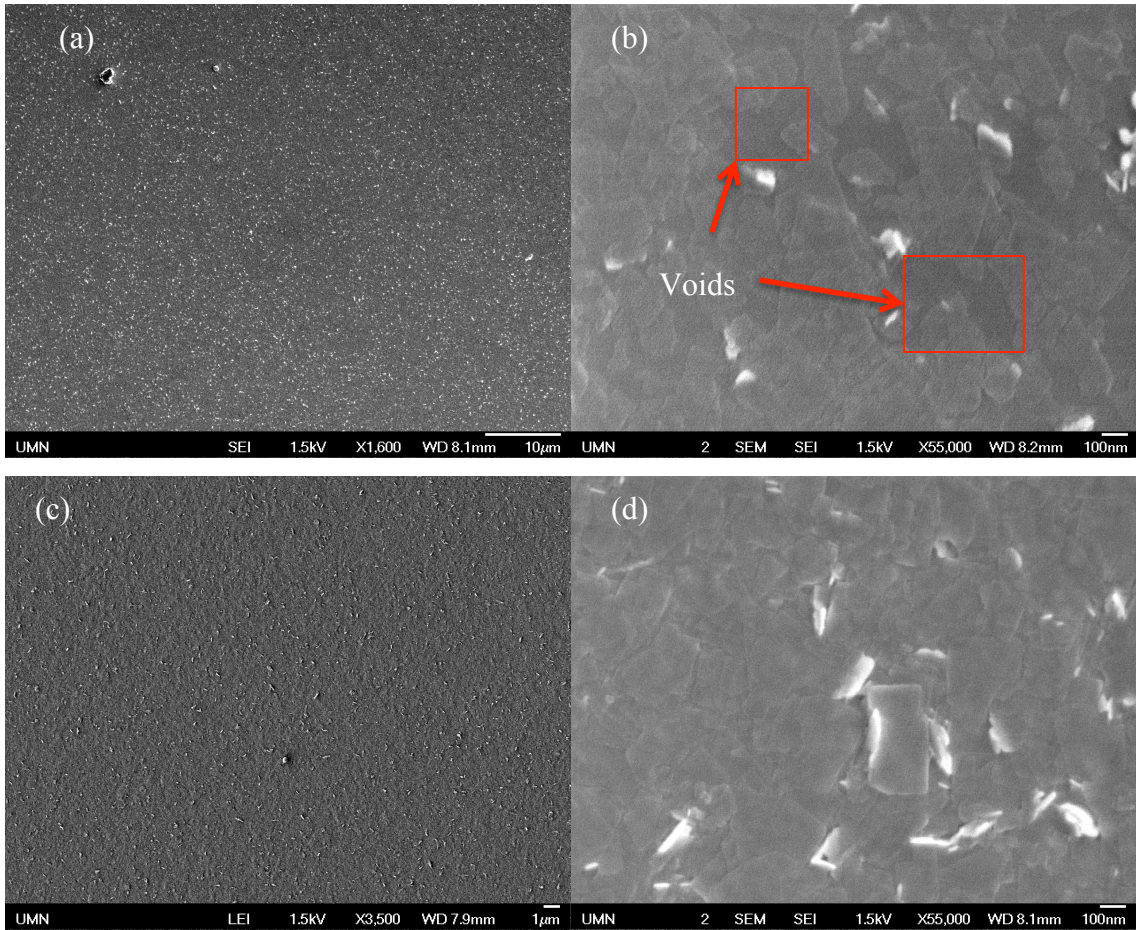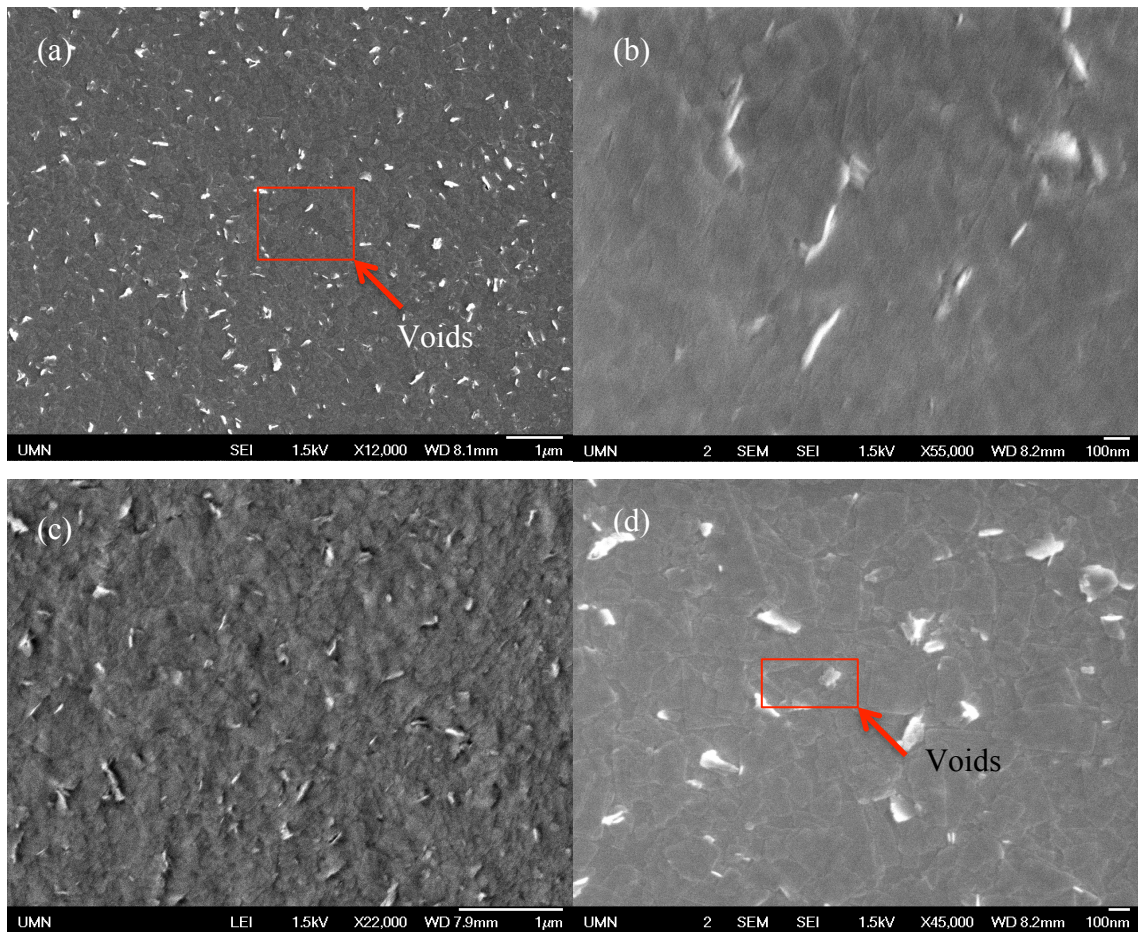
Fig 5.15 SEM images of (a) and (b) along radius area with different magnifications for 1000 rpm coating; (c) and (d) along radius area with different magnifications for 500 rpm coating

**Defects**

Defects can be found in both coatings as shown in Fig 5.16. Some of the defects come from the inward flow as spinning stops, and others may come from disturbance caused by transferring the wet film from the spin coater to the hot plate for drying. Most of the defects are found near the edge area. Therefore, they may not be a big problem if the center area of the films can be maintained.
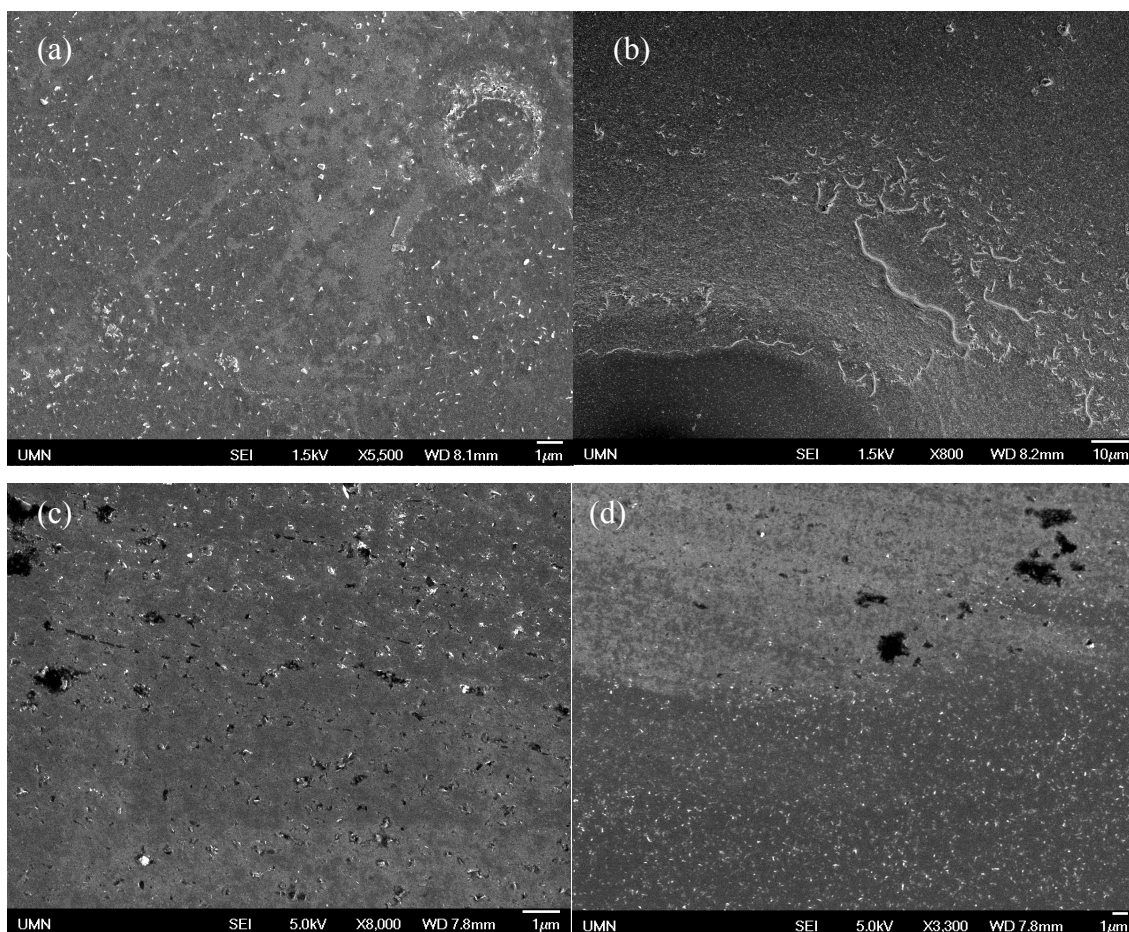
Fig 5.16 SEM images of (a) and (b) defects for 1000 rpm coating (c) and (d) defects for 500 rpm coating

In summary, spin coating offers us uniform and oriented zeolite nanosheets films within a limited range of the substrate. With a higher spin speed, propotion of the uniform area is larger while interparticle gaps within the coating are more likely to apprear.

## 5.4 Comparisons between drop coating and spin coating

With drop coating, all the suspensions delivered on the substrate can be maintained and none of the zeolite nanosheets are wasted. However, because of the low vapor pressure of octanol, drop coating method can take a very long time to dry. Spin coating, on the other hand, is much faster. The problem with this method is that a lot of suspension is wasted

when they fly off the substrate during spin-off stage. Another downside to spin coating is that these coatings can not be made in a roll-to-roll process; instead they have to be batch produced.

From Fig 5.17, with a similar drying temprature, the spin coating films seem to have better orientation than the ones made from drop coating.
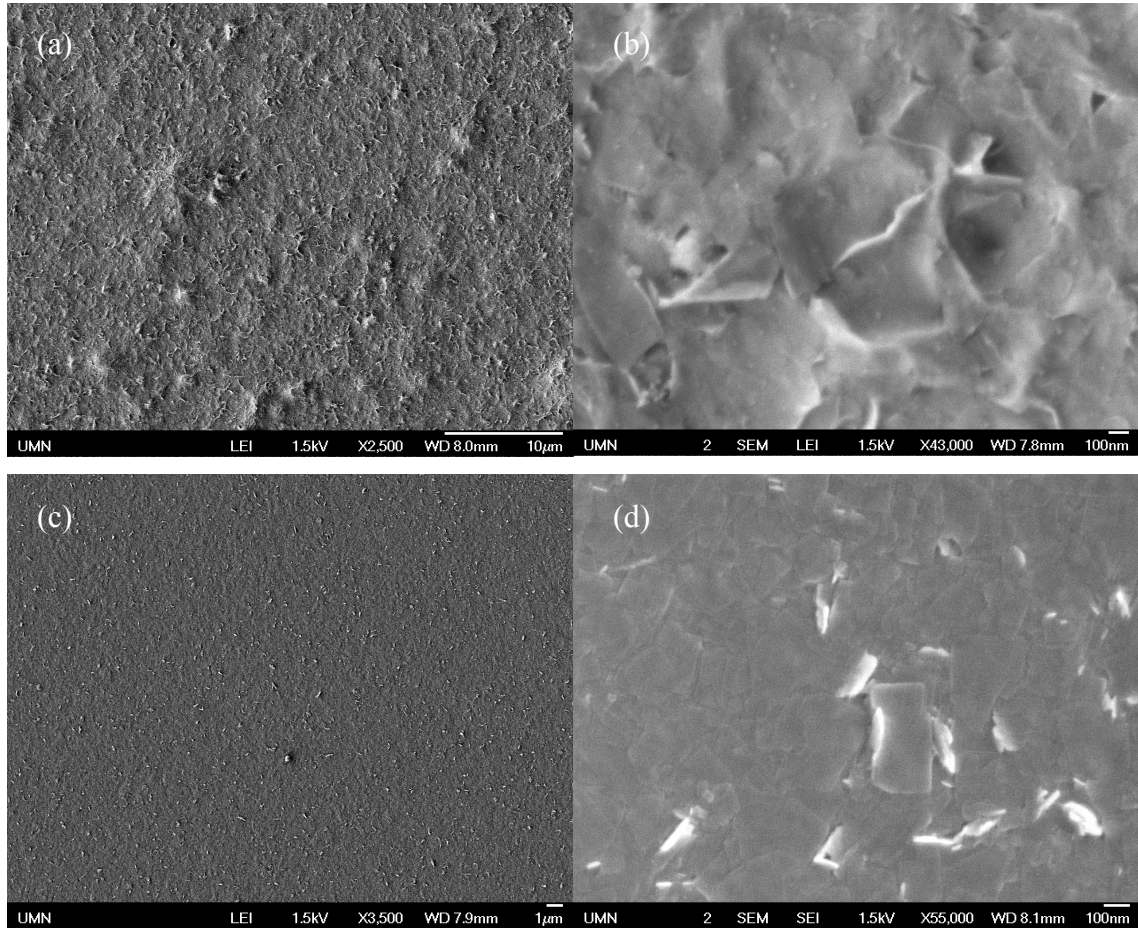


Fig 5.17 SEM images of (a) and (b) center area of drop coating films dried at 32.5℃ (c) and (d) center area of spin coating films with 500 rpm spin rate and dried at 31.8℃

There are two possible explainations to be proposed. One is centirfugal force can act on the zeolite particles and help them orient along the substrate.
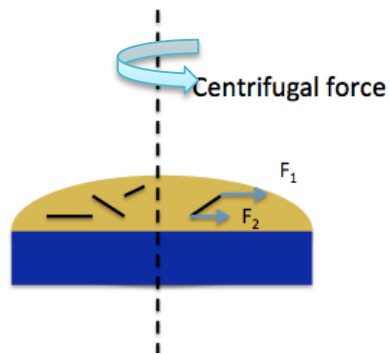
Fig 5.18 Schematic illustration of centrifugal force acting on flate-like particles

The centripetal acceleration is $a = \omega^2 r$, therefore, force acting on the end further from the center is larger than that acting on the end nearer to the center. In Fig 5.18, $F_1$ is larger than $F_2$. The force difference tends to rotate the flate-like particle until it orients parallel to the substrate.

The other way to explain the orientation difference is before drying, spin coating method creates much thinner wet films than the ones made by drop coating. The two wet films have the same concentration assuming that octanol evaporation can be ignored during spinning. A thicker film means more zeolite nanosheets that causes more hinderance for alignment. Orientation uniformity is thus harder to get.

# 6 Summary and future directions

In this work, stable exfoliated zeolite nanosheets suspension has been made for coating processes. Drop coating method and spin coating method have been used to make zeolite nanosheets films. From experimental results, both drop coating method and spin coating method can create a portion of uniform and comparatively oriented zeolite nanosheets films. The films are produced with relatively high thickness compared to those typical of Langmuir-Blodgett deposition method (monolayer), allowing for XRD and SEM characterizations.

Drop coating method can create a much thicker film compared with spin coating method. It can utilize all the zeolite nanosheets that are delivered on the substrates while require a very long drying time when the solvents of the suspension are non-volatile. The film thickness is more uniform in the case of lower drying temperature due to longer sedimentation time and less disalignment effects such as Brownian motion and diffusion. Non-uniform orientation of particles can be easily observed from low-magnification SEM images of films both dried at high temperature and low temperature. The non-uniform orientation may be attributed to a few agglomerated particles or curling of larger nanosheets during deposition.

Spin coating method can create thinner and more oriented films in a shorter period of time compared with drop coating method with a compromise of wasting materials during the spin off stage. The thickness of the films can be predicted using suitable mathematical models from literature. Prediction of film thickness is able to direct the operating conditions such as spin rate and spin time. The films made by the spin coating method generally have a uniform area in the center and a non-uniform area around the edge due to edge effects. For 1000 rpm spin rate and spinning for 1 minute, 59.2% of the one-inch film is uniform. For 500 rpm spin rate and 30 seconds spin time, only 24.1% of the entire film is uniform. With a higher spin rate, the portion of the uniform area increases dramatically as the film thickness decreases. When the spin rate increases to a certain

point, the zeolite nanosheets no longer cover the whole substrate and interparticle gaps appear. Despite the coverage and possible packing issue caused by higher spin rate, the center area of the spin coating films usually has uniform orientation.

Future works can be focused on making low-dielectric materials using these coatings. Secondary growth of the films will be applied to reduce interparticle defects and increase mechanical properties. After secondary growth, dielectric constant can be measured to determine the electric properties of the films. Furthermore, more spin rates or drying temperatures can be tried to create a film with larger uniform area and a better coverage.

# Bibliography

1.  M. Choi, K. Na, J. Kim, Y. Sakamoto, O. Terasaki, and R. Ryoo, 'Stable Single-Unit-Cell Nanosheets of Zeolite Mfi as Active and Long-Lived Catalysts', Nature, 461 (2009), 246-U120.
2.  K. V. Agrawal, B. Topuz, Z. Y. Jiang, K. Nguenkam, B. Elyassi, L. F. Francis, M. Tsapatsis, and M. Navarro, 'Solution-Processable Exfoliated Zeolite Nanosheets Purified by Density Gradient Centrifugation', Aiche Journal, 59 (2013), 3458-67.
3.  X. Y. Zhang, D. X. Liu, D. D. Xu, S. Asahina, K. A. Cychosz, K. V. Agrawal, Y. Al Wahedi, A. Bhan, S. Al Hashimi, O. Terasaki, M. Thommes, and M. Tsapatsis, 'Synthesis of Self-Pillared Zeolite Nanosheets by Repetitive Branching', Science, 336 (2012), 1684-87.
4.  K. Varoon, X. Y. Zhang, B. Elyassi, D. D. Brewer, M. Gettel, S. Kumar, J. A. Lee, S. Maheshwari, A. Mittal, C. Y. Sung, M. Cococcioni, L. F. Francis, A. V. McCormick, K. A. Mkhoyan, and M. Tsapatsis, 'Dispersible Exfoliated Zeolite Nanosheets and Their Application as a Selective Membrane', Science, 334 (2011), 72-75.
5.  L. C. Boudreau, J. A. Kuck, and M. Tsapatsis, 'Deposition of Oriented Zeolite a Films: In Situ and Secondary Growth', Journal of Membrane Science, 152 (1999), 41-59.
6.  Zheng Wang, Ting Yu, Pei Nian, Qingchun Zhang, Junkang Yao, Shan Li, Zuoning Gao, and Xianglong Yue, 'Fabrication of a Highly b-Oriented MFI-Type Zeolite Film by the Langmuir–Blodgett Method', Langmuir, 30 (2014), 4531-4534.
7.  J. Y. Choi, Z. P. Lai, S. Ghosh, D. E. Beving, Y. S. Yan, and M. Tsapatsis, 'Layer-by-Layer Deposition of Barrier and Permselective C-Oriented-Mcm-22/Silica Composite Films', Industrial & Engineering Chemistry Research, 46 (2007), 7096-106.
8.  J. Choi, S. Ghosh, L. King, and M. Tsapatsis, 'Mfi Zeolite Membranes from a- and Randomly Oriented Monolayers', Adsorption-Journal of the International Adsorption Society, 12 (2006), 339-60.
9.  S. Maheshwari, E. Jordan, S. Kumar, F. S. Bates, R. L. Penn, D. F. Shantz, and M. Tsapatsis, 'Layer Structure Preservation During Swelling, Pillaring, and Exfoliation of a Zeolite Precursor', Journal of the American Chemical Society, 130 (2008), 1507-16.
10. A. A. Issa, Y. S. Al-Degs, and N. A. Al-Rabady, 'Deposition of Two Natural Clays on a Pt Surface Using Potentiostatic and Spin-Coating Techniques: A Comparative Study', Clay Minerals, 43 (2008), 501-10.
11. H. Schlicke, J. H. Schroder, M. Trebbin, A. Petrov, M. Ijeh, H. Weller, and T. Vossmeyer, 'Freestanding Films of Crosslinked Gold Nanoparticles Prepared Via Layer-by-Layer Spin-Coating', Nanotechnology, 22 (2011).
12. L. E. Scriven, 'Physics of applications of dip coating and spin coating', Materials Research Socienty Spring Symposium, 1988
13. D. E. Bornside, 'Spin coating', PhD Thesis, University of Minnesota, 1988.
14. C. J. Lawrence, 'The Mechanics of Spin Coating of Polymer-Films', Physics of Fluids, 31 (1988), 2786-95.
15. Alfred G. Emslie, Francis T. Bonner, and Leslie G. Peck, 'Flow of a Viscous Liquid on a Rotating Disk', Journal of Applied Physics, 29 (1958), 858-62.

16. T. J. Rehg, and B. G. Higgins, 'Spin Coating of Colloidal Suspensions', Aiche Journal, 38 (1992), 489-501.
17. D. E. Bornside, C. W. Macosko, and L. E. Scriven, 'Spin Coating - One-Dimensional Model', Journal of Applied Physics, 66 (1989), 5185-93.
18. D. B. Hall, P. Underhill, and J. M. Torkelson, 'Spin Coating of Thin and Ultrathin Polymer Films', Polymer Engineering and Science, 38 (1998), 2039-45.
19. D. E. Bornside, C. W. Macosko, and L. E. Scriven, 'Spin Coating of a Pmma Chlorobenzene Solution', Journal of the Electrochemical Society, 138 (1991), 317-20.
20. D. Meyerhofer, 'Characteristics of Resist Films Produced by Spinning', Journal of Applied Physics, 49 (1978), 3993-97.
21. A. Iguchi, K. Komori, and R. Izumi, 'Characteristics of Heat and Mass-Transfer from a Rotating-Disk with Sink Flow', International Journal of Heat and Mass Transfer, 22 (1979), 1319-21.
22. P. Z. Sun, R. Z. Ma, K. L. Wang, M. L. Zhong, J. Q. Wei, D. H. Wu, T. Sasaki, and H. W. Zhu, 'Suppression of the Coffee-Ring Effect by Self-Assembling Graphene Oxide and Monolayer Titania', Nanotechnology, 24 (2013).
23. R. D. Deegan, O. Bakajin, T. F. Dupont, G. Huber, S. R. Nagel, and T. A. Witten, 'Capillary Flow as the Cause of Ring Stains from Dried Liquid Drops', Nature, 389 (1997), 827-29.
24. R. D. Deegan, O. Bakajin, T. F. Dupont, G. Huber, S. R. Nagel, and T. A. Witten, 'Contact Line Deposits in an Evaporating Drop', *Physical Review E,* 62 (2000), 756-65.
25. E. G. Shafrin, W. A. Zisman, 'Constitutive relations in the wetting of low energy surfaces and the theory of the retraction method of preparing monolayers', The Journal of Physical Chemistry, 64 (1960), 519-524
26. N. Eustathopoulos, M. G. Nicholas, B. Drevet, 'Wettability at high temperatures', Materials and Corrosion, 51 (2000), 666.
27. T. Young, 'An essay on the cohesion of fluids', Philosophical Transactions of the Royal Society of London, 95 (1805), 65-87.
28. D. Griese, 'Distribution and orientation of non-spherical particles in drying particulate coatings', Thesis, University of Minnesota, 2013.
29. E. Kirchner, 'Film Shrinkage and Flake Orientation', Progress in Organic Coatings, 65 (2009), 333-36.
30. G. K. Batchelor, 'The effect of Brownian motion on the bulk stress in a suspension of spherical particles', Journal of Fluid Mechanics, 83 (1977), 97-117.
31. C. F. Yang, W. H. Smyrl, and E. L. Cussler, 'Flake Alignment in Composite Coatings', Journal of Membrane Science, 231 (2004), 1-12.
32. E. Suzuki, 'High-Resolution Scanning Electron Microscopy of Immunogold-Labelled Cells by the Use of Thin Plasma Coating of Osmium', Journal of Microscopy-Oxford, 208 (2002), 153-57.
33. B. O. Dabbousi, J. RodriguezViejo, F. V. Mikulec, J. R. Heine, H. Mattoussi, R. Ober, K. F. Jensen, and M. G. Bawendi, '(Cdse)Zns Core-Shell Quantum Dots: Synthesis and Characterization of a Size Series of Highly Luminescent Nanocrystallites', Journal of Physical Chemistry B, 101 (1997), 9463-75.

34. N. F. Cheville, and J. Stasko, 'Techniques in Electron Microscopy of Animal Tissue', Veterinary Pathology, 51 (2014), 28-41.
35. D. B. Williams, C. B. Carter, 'Transmission electron microscopy', Springer, 2009
36. R. F. Egerton. 'Physical principles of electron microscopy: an introduction to TEM, SEM, and AEM', Springer, 2005.
37. R. Feidenhansl, 'Surface-Structure Determination by X-Ray-Diffraction', Surface Science Reports, 10 (1989), 105-88.
38. W. H. Bragg, 'The investigation of the properties of thin films by means of X-rays', Proceedings of the Royal Institution of Great Britain, 16 (1925), 1-10.
39. S. Kobayashi, 'X-ray thin-film measurement techniques IV. In-plane XRD measurements', The Rigaku Journal, 26 (2010), 3-11.
40. International Zeolite Association, http://www.iza-online.org/, 2014.
41. G. T. Kokotailo, S. L. Lawton, D. H. Olson, D. H. Olson, and W. M. Meier, 'Structure of Synthetic Zeolite Zsm-5', Nature, 272 (1978), 437-38.
42. J. Caro, and M. Noack, 'Zeolite Membranes - Recent Developments and Progress', Microporous and Mesoporous Materials, 115 (2008), 215-33.
43. A. Corma, V. Fornes, S. B. Pergher, T. L. M. Maesen, and J. G. Buglass, 'Delaminated Zeolite Precursors as Selective Acidic Catalysts', Nature, 396 (1998), 353-56.
44. Mark A Snyder, and Michael Tsapatsis, 'Hierarchical Nanomanufacturing: From Shaped Zeolite Nanoparticles to High-Performance Separation Membranes', Angewandte Chemie International Edition, 46 (2007), 7560-73.
45. S. Maheshwari, E. Jordan, S. Kumar, F. S. Bates, R. L. Penn, D. F. Shantz, and M. Tsapatsis, 'Layer Structure Preservation During Swelling, Pillaring, and Exfoliation of a Zeolite Precursor', Journal of the American Chemical Society, 130 (2008), 1507-16.
46. R. A. Vaia, K. D. Jandt, E. J. Kramer, and E. P. Giannelis, 'Kinetics of Polymer Melt Intercalation', Macromolecules, 28 (1995), 8080-85.
47. E. Manias, A. Touny, L. Wu, K. Strawhecker, B. Lu, and T. C. Chung, 'Polypropylene/Montmorillonite Nanocomposites. Review of the Synthetic Routes and Materials Properties', Chemistry of Materials, 13 (2001), 3516-23.
48. T. G. Pretlow, and T. P. Pretlow, 'Velocity Sedimentation of Cells', Nature, 333 (1988), 97-97.
49. P&R Labpak limited, http://prlabpak.blogspot.com/2013/04/hydrofluoric-acid.html, 2014.
50. K. Hermansson, 'Wetting properties of silicon surfaces', Solid-state sensors and actuators, International conference, 1991, 193-196.
51. A. Corma, 'Materials Chemistry Catalysts Made Thinner', Nature, 461 (2009), 182-83.